A newly discovered major Proterozoic granite-alteration system in the Mount Webb region, central Australia, and implications for Cu–Au mineralisation

Lesley Wyborn[1], Murray Hazell[1], Rod Page[1], Mart Idnurm[1], & Shen-su Sun[1]

The presence of a major granite-related alteration system has been confirmed in the western Arunta Block — in the remote Mount Webb region (WA/NT border; Fig. 1). According to al. (1977: BMR Bulletin 197) suggested that the Mount Webb Granite and felsic volcanics of the adjacent Pollock Hills Formation potentially had primary and

Fig. 1. Location of the Mount Webb region, western Arunta Block.

new petrological, geochemical, and geochronological data from the Mount Webb Granite and its comagmatic felsic volcanics in the Pollock Hills Formation, this magmatic system has many similarities to granites in other Australian Proterozoic regions where hydrothermal Cu and or Au deposits have been linked to magmatic sources (e.g., eastern Mount Isa Inlier, Gawler Craton). Key criteria that establish this region as prospective are:

- fractionation trends in the granite, clearly evident in the geochemical data;
- magmatic alteration effects (including sodic–calcic, sericitic, and hematite–K-feldspar) in the granite and country rock; and
- evidence of metallogenically significant hydrothermal interaction with the country rock.

A preliminary interpretation of the results of 12 analyses recorded in AGSO's ROCKCHEM database and in Blake et

alteration characteristics similar to granites of the metallogenically important Williams Batholith (eastern Mount Isa Inlier) and Hiltaba Suite (Gawler Craton), both of which are closely associated with Cu–Au mineralisation (Wyborn 1994: Centre for Ore Deposit & Exploration Studies, University of Tasmania, Master of Economic Geology Course, Manual 2). Reference to '… thicker quartz veins cutting highly altered and brecciated granite west of Pollock Hills' (Blake & Towner 1974: BMR Record 1974/53) further heightened the intrigue. In May 1996, AGSO staff visited the Mount Webb region to collect a suite of samples (Fig. 2) for magma typing, age determination, and alteration mapping and evaluation.

The results described here focus on the Webb 1:250 000 Sheet area, but the granite system extends westward into the Wilson Sheet area, and eastward into the Macdonald, Mount Rennie, and possibly Mount Liebig Sheet areas (Fig. 1). Both

the granite system and the alteration are large by Australian Proterozoic granite standards.

Petrological data

Country rock

In the Webb Sheet area (Blake & Towner 1974: op. cit.; Blake 1977: Webb 1:250 000 Geological Series —explanatory notes, BMR/AGSO), the Mount Webb Granite intrudes 'unnamed Archaean?' rocks (mainly interbedded quartzite and mica schist, and some amphibolite). Near the inferred contact between granite and amphibolite at the southernmost part of one Archaean? outcrop at Pokali Hills (20 km east of Mount Webb), quartz veins and minor ironstones are prominent, and so too is an overprint (metasomatic?) of quartz, biotite, and magnetite replacing all the primary minerals. Away from the inferred contact, constituents of the country rock in this outcrop are mainly amphibole and plagioclase in the central part, and chlorite, actinolite, and minor greenish biotite in the north, suggesting that the granite has both contact-metamorphosed and metasomatically altered the country rock. The country rock elsewhere in the Sheet area is dominated by quartzite and mica schist; late-stage quartz and quartz–tourmaline veins are abundant, and the rock is locally brecciated (Blake & Towner 1974: op. cit.).

Mount Webb Granite

The Mount Webb Granite is hetero-geneous, comprising several types of unaltered granite, sodic–calcic-altered granite, sericite-altered granite, and aplite. Most altered samples are from near the Mount Webb Shear Zone (Fig. 2). All samples are recrystallised, and most have a distinct foliation, suggesting that the granite has been affected by a post-intrusion metamorphic event.

Essentially ***unaltered granite*** ranges from mafic diorite/tonalite through granodiorite, monzogranite (dominant), and syenogranite, to aplite. Some late felsic fractionated phases contain fluorite and nodules of tourmaline ± quartz. These rocks have a typical I-type mineralogy, and are composed of hornblende, biotite, magnetite, plagioclase, K-feldspar, and quartz. Magnetite, generally with exsol-
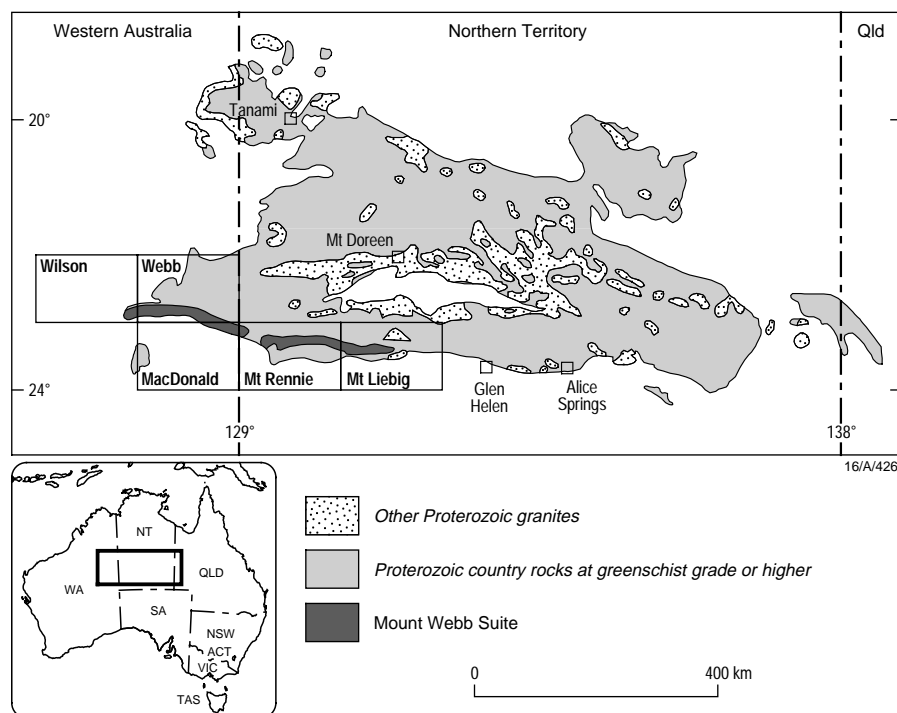
ution lamellae of ilmenite, is common in most samples, but is more abundant in the diorite/tonalite; sulphides are extremely rare. Rimming of the magnetite by titanite is one of the tangible effects of alteration.

Sodic–calcic alteration is characterised by the assemblage diopside + epidote ± tremolite (only present in the more deformed samples). This alteration type is prominent in a linear shear zone trending 310° both to the northwest and southeast of Mount Webb. Few quartz veins bisect the rocks affected by this alteration type, and open spaces were not observed. Most samples contain titanite, and have albite/oligoclase as their only feldspar. Neither sulphides nor anomalous concentrations of elements are apparent in the samples.

Sericite alteration is more restricted than the sodic–calcic alteration, and is usually associated with brecciated and fractured granite cut by quartz veins with open spaces. A higher modal abundance of sulphides accompanies this type of alteration. In thin section, the sericite consists mainly of fine grains concentrated in veins aligned parallel to the foliation. Opaque phases are rare: some samples have magnetite or small pyrite grains; one has chalcopyrite. Two weathered samples containing visible malachite have Cu concentrations of 348 and 278 ppm; thin sections show that they consist mainly of goethite, which was probably formed as a weathering product of primary sulphides.

Quartz veins carrying sulphides are more prominent in the areas of sericitic alteration, where the granite also tends to be more brecciated and bears tourmaline and fluorite. The sulphides are mainly pyrite, though galena was observed in one sample with 1800 ppm Pb, and another sample has 145 ppm Mo.

Aplite veins, common in the more felsic granite, are probably the products of late-stage magmatic processes.

Pollock Hills Formation

The felsic volcanics of the Pollock Hills Formation consist mainly of black porphyritic dacite and rhyodacite overlain by tuffaceous and non-tuffaceous sedimentary rocks (Blake & Towner 1974: op. cit). Alteration is less pervasive in the volcanics than in the Mount Webb Granite, and two alteration types are evident: hematite and epidote. Overall, even the least altered volcanic samples have a markedly recrystallised texture in thin section, suggesting that they are metamorphosed.

The *least altered volcanics* are mainly porphyritic ignimbrites with phenocrysts of plagioclase, magnetite, and quartz in decreasing order of abundance. Phenocrysts of ferromagnesian silicate minerals (altered to epidote and/or biotite) are rare. The ignimbrites comprise two broad types: those with abundant lithic fragments and crystals, and those with a lower crystal and lithic content. The lithic-poor ignimbrites contain flattened pumice clasts and abundant spherulites in the matrix; the spherulites indicate that the matrix comprises devitrified volcanic ash. Lapilli tuffs were observed at one locality. Fine-grained magnetite is scattered throughout the groundmass, which is commonly recrystallised. Although, small grains of pyrite/chalcopyrite occur in the spherulite-bearing volcanics, most of the

volcanics have magnetite as the dominant opaque mineral; primary sulphides are rare, reflecting the high oxidation state of the magma.

Hematite alteration in the volcanics is possibly related to two events. Firstly, as noted by Blake & Towner (1974: op. cit.), hematite alteration is more prominent at the top of the volcanics, near their contact with the sedimentary rocks of the Pollock Hills Formation. Red hematite-rich layers interspersed with these sedimentary rocks suggest that oxidising atmospheric conditions prevailed during sedimentation and extrusion, so the hematite may be related to meteoric fluids rather than to hydrothermal/magmatic processes. Some

of this early hematitic alteration is also cut by late epidote alteration.

Secondly, hematite alteration is evident in highly sheared volcanics sampled away from the sediment/volcanic interface. At one locality, northwest of Kiwirrkurra, a hematite-rich, K-feldspar-altered volcanic rock associated with an
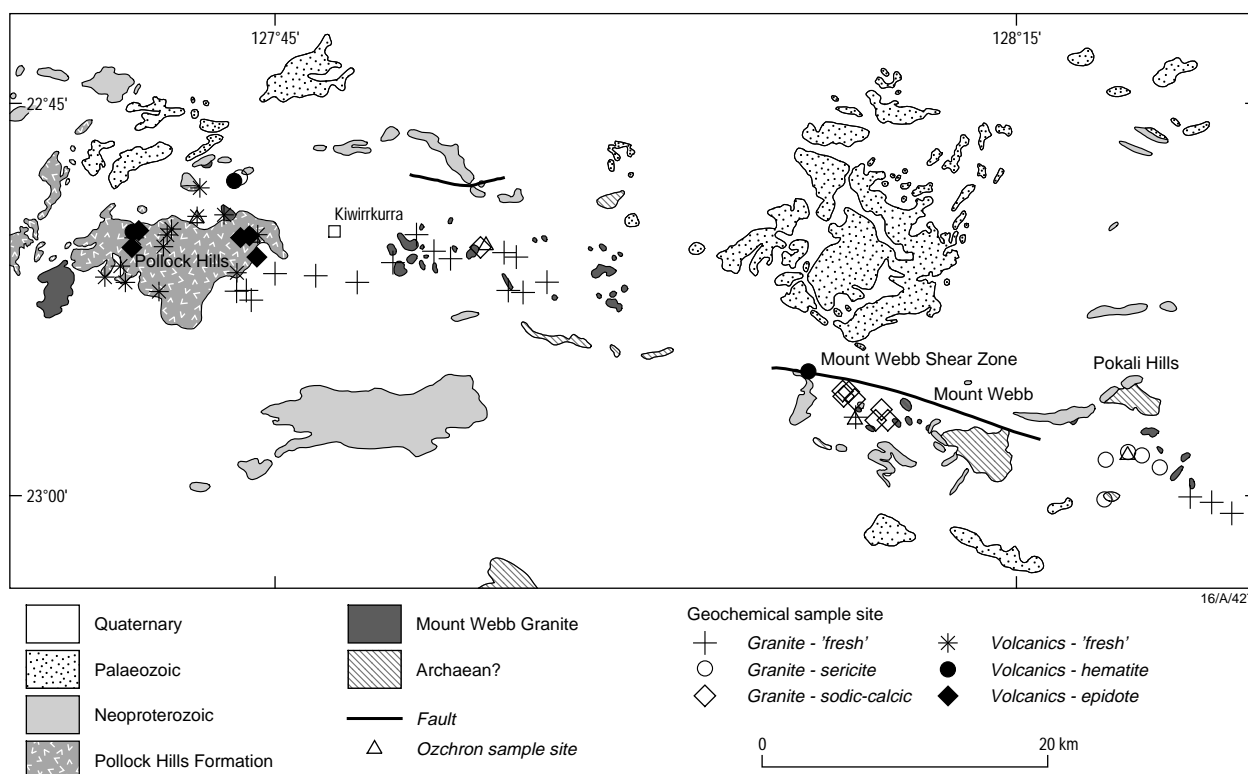

Fig. 2. Geology of the Mount Webb region (based on Blake 1977: op. cit.).

ironstone cuts a chlorite/sericite-altered volcanic rock, and is therefore later in the paragenesis. At another, an isolated

volcanic outcrop northwest of Mount Webb, hematite alteration is also apparent in a sample of K-feldspar-bearing rock containing anomalously high potassium. Shearing at both localities suggests that

this type of hematite alteration is due to another event, distinct from that formed at the sediment/water interface early in the paragenetic history.

Epidote alteration is common in the volcanics. In thin section, it is pervasive and texturally destructive. It progressively destroys any original igneous textures, and produces an end-member assemblage

of epidote + quartz. Mineralogically and chemically it closely resembles the sodic–calcic alteration of the Mount Webb Granite, and both are focused in shear zones trending ca 310°.

Mafic dykes

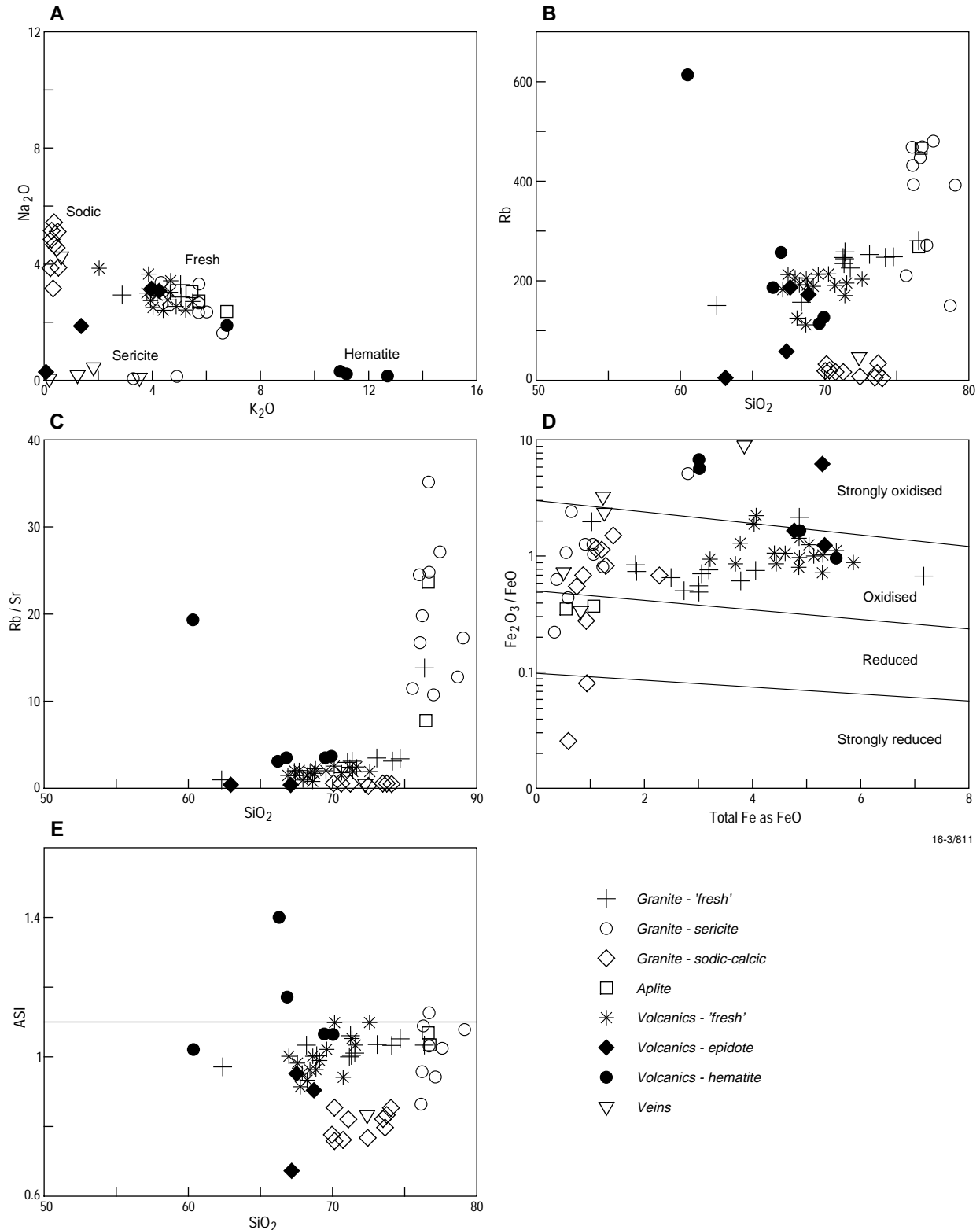Mafic dykes with a prominent north-northwesterly trend are prominent in the

Fig. 3. Geochemical variation diagrams for whole-rock geochemical data from the Mount Webb region.

Table 1. Summary of new U–Pb SHRIMP and Sm–Nd results from the Mount Webb region

Sample no.	Rock unit	Rock type	SiO_2	Age (Ma)	Xenocrysts	εNd_i	T_{DM} (Ma)
96496035	Mount Webb Granite	monzogranite	74 wt %	1643 ± 4	1680–1690 Ma (4 grains), ~1775 Ma (2 grains), 1860–1870 Ma (2 grains)	–2.1	2327
96496028A	Mount Webb Granite	granodiorite	68 wt %	1639 ± 5	1690 Ma (1 grain)	–2.0	2322
96496011	Mount Webb Granite	sericite-altered granite	77 wt %	1639 ± 5	Complex with inheritance patterns at ~1680, ~1760, and 1830–1877 Ma		
96496024	Pollock Hills Formation	lithic-rich ignimbrite	68 wt %	1643 ± 13 (NB: one grain only)	Complex populations 1680–1690, 1862 ± 4 (dominant), single grains at 1966, 2590 Ma	–1.5	2325
96496009	unnamed dolerite	dolerite	48 wt %	976 ± 3 (zircon) 972 ± 8 (baddelyite)	~1630 Ma	2.3	

area, particularly in the granite outcrops east of the Pollock Hills, but do not intrude the Neoproterozoic and younger sequences (Blake 1977: op. cit.). In thin section, most appear to be pristine, consisting of plagioclase, clinopyroxene, and orthopyroxene; they also contain sulphides (mostly pyrite, but some chalcopyrite). A few of them evince pronounced alteration effects, and are probably older, but they all lack deformational and metamorphic effects, suggesting that they are much younger than the granite.

Geochemistry results

Sixty samples were collected for analysis: 28 granites, nine aplites and quartz veins, 18 volcanic rocks, and five dolerites. The alteration effects in the granites and volcanics are clearly shown in a plot of Na_2O vs K_2O (Fig. 3A). The sodic–calcic-altered samples are depleted in K_2O, whereas the more strongly sericite-altered samples have lost Na_2O. In contrast, the hematite-altered samples show a marked enrichment in K_2O, similar to that in the ~1500-Ma granites in the Cloncurry district (Wyborn in press: Australian Journal of Earth Sciences).

The plots for Rb and Rb/Sr show exponentially increasing values with increasing SiO_2 (Figs. 3B and C). On the Fe_2O_3/FeO vs total Fe as FeO plot (Fig. 3D) of Champion & Heinemann (AGSO Record 1994/11), most samples lie in the oxidised field. The ASI values (molecular $Al_2O_3/[K_2O + \{CaO - 1/3P_2O_5\} + Na_2O]$) are <1.1, indicating that the samples are metaluminous to weakly peraluminous. All these features are characteristic of granites associated with Cu–Au mineralisation in the Proterozoic (see also Wyborn 1994: Geological Society of Australia, Abstracts, 37, 471–472.)

Geophysical data

Parts of the hydrothermal alteration system occur in the Webb and Wilson Sheet areas, for which no airborne geophysical data are in the public domain. We recorded ground magnetic observations on a Geoinstruments susceptibility meter (model JH–8). Susceptibilities range from 200 to 600 SI units $\times 10^{-5}$ for the (dominant) monzogranite, and 2000–5000 SI units x 10^{-5} for the tonalite/diorite, reflecting increasing modal abundance of magnetite with decreasing SiO_2. The felsic volcanics also have high susceptibilities, generally from 3000–5000 SI units x 10^{-5}, mirroring the abundant magnetite phenocrysts and the ubiquitous fine-grained magnetite in the groundmass.

Alteration zones in both the granite and the volcanics have much lower magnetic susceptibilities (generally <40 SI units x 10^{-5}), reflecting the destruction of magnetite in the areas of sodic–calcic alteration. Although magnetite is generally absent from the sericite-altered areas, some high-susceptibility localities are apparent there.

The country rock generally has low measured susceptibilities, except amphibolite in the Pokali Hills area, where susceptibilities are variable and range from 200–5000 SI units x 10^{-5}. Those rocks with particularly high susceptibilities had metasomatic biotite and magnetite in thin section. The fresh mafic dykes, including the dated sample, have high susceptibilities (>4000 SI units x 10^{-5}); altered dykes have low susceptibilities.

Geochronology results

Page et al. (1976: BMR Journal of Australian Geology & Geophysics, 1, 1–13) obtained a combined Rb–Sr isochron age of 1494 ± 25 Ma (recalculated with the 1.42 x 10^{-11} yr^{-1} constant for Rb^{87}) and an initial Sr^{87}/Sr^{86} ratio of 0.7114 ± 0.004 for the Pollock Hills Formation and
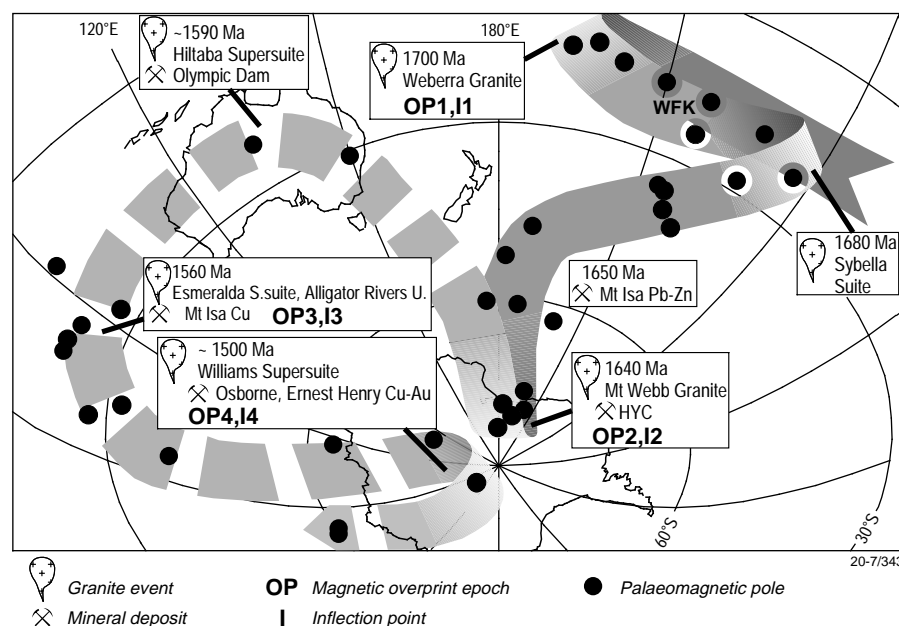
Fig. 4.

The Proterozoic APWP for Australia showing the locations of palaeomagnetic poles. Major granite and ore deposit events are also shown (based on Loutit et al. 1994: op. cit.).

Mount Webb Granite. Such a high initial ratio for an I-type granite suggests that the Rb–Sr data have been reset, so samples (five) were selected for SHRIMP U–Pb zircon dating (Table 1).

The three granite samples yield ages of 1643 ± 4, 1639 ± 5, and 1639 ± 5 Ma, indicating that they all belong to the one magmatic system. Inherited zircon populations include 1680–1690, 1775–1769, and 1830–1877 Ma. A corollary to these results is that the anomalously young Rb–Sr age might reflect the ubiquitous late metamorphic overprint of both the volcanics and granite.

No satisfactory igneous crystallisation age was obtained for the volcanics of the Pollock Hills Formation, as the zircon populations in the sample studied are exceedingly complex. This sample is dominated by inherited ~1860-Ma zircon; a population at ~1680–1690 Ma is also prominent; older inheritance at ~1970 Ma and 2590 Ma is also apparent. These populations are distinctly older than those of the granite; only one grain analysed from the volcanic sample was close to the age of the granite (~1640 Ma). The dated sample has abundant lithic fragments, and is likely to have xenocrystic zircon populations derived from these fragments. Jagodzinski (1992: AGSO Record 1992/9; see also pp. 23–25 in this newsletter) has reported a similar case in the Coronation Hill region (NT), where an ignimbrite dominated by lithic fragments yielded mainly xenocrystic zircon populations and only a few magmatic grains.

Nd isotopic data from the samples of the Mount Webb Granite and volcanics gave εNd$_i$ values of –1.5 to –2.1 and single-stage T$_{DM}$ model ages of ~2320 Ma (Table 1), similar to those obtained elsewhere in the Arunta Block (Sun et al. 1995: Precambrian Research, 71, 301–314). They indicate that the felsic magmas were derived from a pre-existing crustal source.

Both magmatic zircon and baddelyite were dated from an unmetamorphosed dolerite dyke. They recorded Neoproterozoic ages of 976 ± 3 and 972 ± 8 Ma respectively, dispelling the notion of any connection between the dykes and the Mount Webb Granite. These dykes are considerably younger than the Stuart Pass Dolerite, which is abundant throughout the Arunta Inlier and has a well-defined Sm–Nd mineral isochron age of 1076 ± 33 Ma (Zhao & McCulloch 1993: Chemical Geology, 109, 341–354).

Implications of the 1640-Ma age for the Mount Webb Granite

The new age for the Mount Webb Granite is similar to the 1640 ± 7-Ma age of tuffs in the HYC orebody at McArthur River (Page & Sweet in press: Australian Journal of Earth Sciences). Although the similarity may be purely coincidental (not all tuffs in the north Australian Proterozoic sequences have known Australian sources), it does raise the possibility that the HYC tuffs were derived from the Mount Webb region, especially considering the size of the intrusive event.

It is interesting to note that Loutit et al. (1994: Australasian Institute of Mining & Metallurgy, Publication Series, 5/94, 123–128) observed that most major granite and major ore-forming events correspond to major inflections in the Australian apparent polar-wander path (APWP; Fig. 4). However, no major granite event was then known to correspond to the major hairpin bend at ~1640 Ma. The new data from the Mount Webb Granite provide evidence for such an event. Loutit et al. (1994: op. cit.) asserted that APWP inflections correspond to changes in the direction of crustal plate movement and, therefore, changes in the stress field within the plate. Such changes in stress could allow granitic melts to ascend from the lower crust, explaining the formation of major batholiths at these times.

Mineral potential of the Mount Webb region

Although the present results are preliminary, the primary and alteration geochemistry of the felsic magmas of the Mount Webb region resemble those of other Proterozoic Cu–Au mineralised areas. There is evidence of extensive magmatic alteration (sodic–calcic and sericitic) at some localities, particularly within the more felsic varieties of the granite. Within the sericite-altered granites, fluorite, tourmaline, and sulphides are common accessories, and some of the samples have anomalous F, Cu, and S. Cross-cutting veins also have elevated Mo and Pb values. There is also evidence of metasomatic alteration of the adjacent country rock.

Recent exploration results have confirmed that this truly 'greenfield' area may have some economic significance. Semicontinuous rock-chip sampling returned results of 9.1% Cu, 3 g/t Ag, and 0.38 g/t Au over a true width of 4 m, and 0.3% Cu and 8 g/t Ag over a true width of 10 m. An aircore-drilling program has confirmed the presence of three Cu–Au–Ag anomalous areas, of which the largest returned peak values of 0.21 ppm Au and 896 ppm Cu on three adjacent 800-m-spaced grid lines (Aurora Gold Ltd, quarterly report, December 1997).

Acknowledgments

A Mesoproterozoic palaeomagnetic age for the gold-bearing Quamby Conglomerate, Queensland

Mart Idnurm[1] & Lesley Wyborn[1]

The Quamby gold deposit in the Eastern Fold Belt of the Mount Isa Inlier is hosted by the Quamby Conglomerate. This fold belt also contains several Cu–Au deposits, including the major Ernest Henry deposit ~40 km east of Quamby, which are believed to have been formed by hydrothermal processes related to the intrusion of the nearby ~1500-Ma Williams and Naraku batholiths. The genetic link between the Quamby deposit and the others is not clear, partly because the age of the conglomerate has remained uncertain. We describe here the results of palaeomagnetic dating of the conglomerate, which was carried out to help understand the origin of the Quamby deposit and gold mineralisation in the Eastern Fold Belt in general.

contains the deposit, is bounded by the Mount Rosebee and Camel Creek Faults; the southern block lies within the Quamby Fault Zone. Although tightly folded at some localities, the unit contains no evidence of metamorphism; its maximum age, therefore, is ~1550–1500 Ma — the end of the last period of regional metamorphism in the Mount Isa Inlier. The Late Proterozoic and Phanerozoic previously have been tentatively suggested for its age (e.g., Connor et al. 1990, in F.E. Hughes, Editor: Mineral deposits of Australia and Papua New Guinea, Australasian Institute of Mining & Metallurgy, Melbourne, 949–953; Derrick 1980: Marraba, Queensland, 1:100 000 Geological Map Commentary, BMR/AGSO).

comprising normally 26 heating steps in the range 100–695°C, were used for analysing the components of remanence.

The magnetisation intensity of the typical arenite sample changed little up to at least 600°C, and with few exceptions the arenite remanences contained a single component. Figure 6A shows the site mean directions for that component together with the 95% confidence circles. Corrections for bedding dips halved the directional scatter, indicating that the magnetisation was acquired before deformation. Eleven of the twelve site mean directions form a pair of antipolar groups that represent either identical or closely similar ages. The twelfth direction (marked X in Fig. 6A) cannot be assigned to either group, and does not correspond to any part of the Australian apparent polar-wander path (APWP). (The cause of the discrepancy is not clear; it may be due, for example, to unrecognised structural complexity at the site.) Discarding the discrepant direction and assigning equal weights to the eleven concordant directions produces an overall mean direction of declination 3.9° and inclination $-31.2°$ ($\alpha_{95} = 5.5°$). This equates to a palaeomagnetic pole at latitude 85.0°S and longitude 7.4°E ($A_{95} = 5.4°$), labelled QC on the APWP (Fig. 7).

Although the remanences of the slate cobbles are poorly defined, most reveal two components. The first demagnetised in the hematite temperature range well above the Curie point of magnetite (580°C), and yielded random directions, as expected for the magnetisation of cobbles deposited in random orientations. The second component unblocked below the Curie point of magnetite. Its directions, although highly scattered, are not random (Fig. 6B). Part of the scatter may be due to the presence of the higher-temperature random component, which may not have been completely eliminated by demagnetisation. The mean field-corrected direction for this component is declination 307.8°, inclination 39.6° ($\alpha_{95} = 22.9°$), equating to a pole (QCC in Fig. 7) at latitude 21.4°S and longitude 269.2°E ($A_{95} = 22.9°$). In view of the poor quality of the results and the large scatter among sample directions, this pole should be regarded as only a rough approximation.
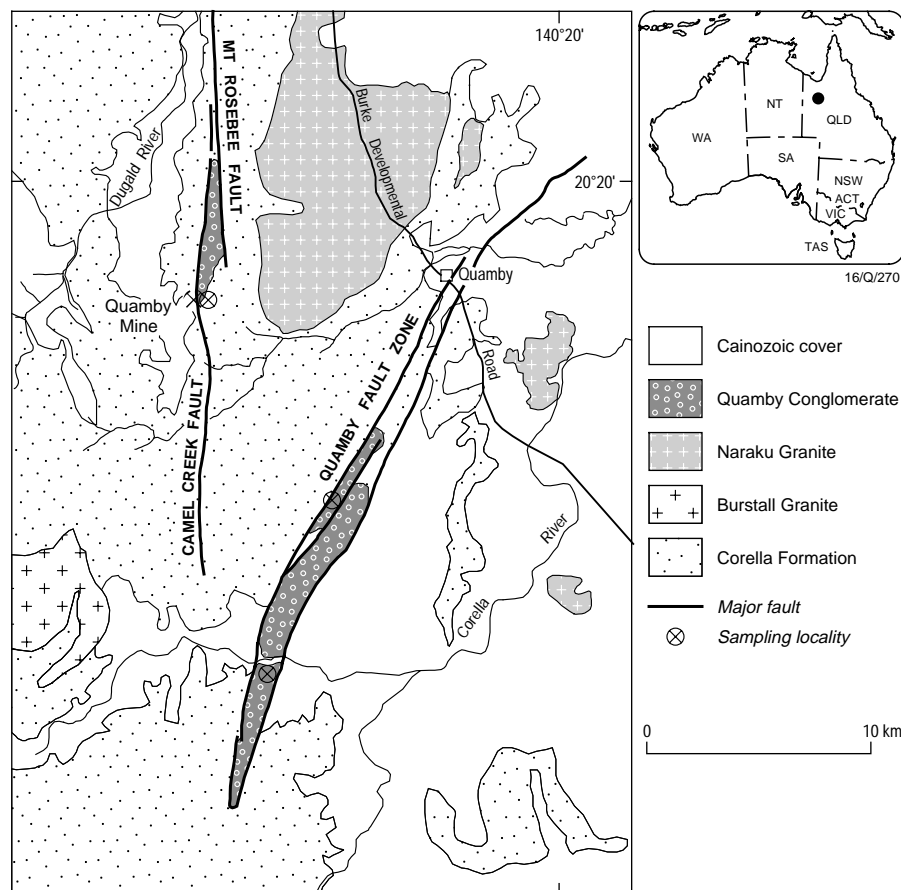

Fig. 5. Simplified geological setting of the Quamby Conglomerate, and sampling localities.

The Quamby Conglomerate comprises mainly conglomerate, feldspathic sandstone, and greywacke. Clasts include slate, schist, and quartzite. Hematite is ubiquitous, and is regarded as postdepositional, possibly of hydrothermal origin. The unit crops out in two northerly and north-northeasterly trending graben-like structures (Fig. 5), where it is unconformably underlain by metasediments mapped as the Palaeoproterozoic Corella Formation. The northern block, which

Palaeomagnetic techniques

We collected 110 oriented samples from red arenite lenses and the least pebbly beds at twelve spot localities in the northern and southern blocks. Forty-nine other samples were obtained from cobbles of slate within the conglomerate, to check that their remanences have random directions (i.e., are not postdepositional overprints). Standard thermal demagnetisation techniques,

Age of the Quamby Conglomerate

The pole QC for the Quamby Conglomerate plots on the Australian APWP near but on the younger side of the pole IM, which represents the final stages of metamorphism in the Mount Isa Inlier. This is consistent with sedimentation of the Quamby Conglomerate postdating regional metamorphism. The closeness of the two poles suggests that the hematite was introduced soon after the

metamorphism. Therefore, the age of the unit is inferred to be ca 1500 Ma, which leaves open two interpretations for the origin of the gold.

Firstly, this age corresponds to the period of widespread circulation of hydrothermal fluids that probably produced the Cu–Au deposits in the Eastern Fold Belt (Perkins & Wyborn 1996: AGSO Research Newsletter, 25, 8–9). In view of the proximity of the Mount Rosebee and Camel Creek Faults, these fluids may account for both the gold and secondary hematite in the unit. We note a similar association of gold with chemically deposited hematite at Ernest Henry (Craske 1995: Australian Institute of Geoscientists [AIG], Bulletin, 16, 95–109).
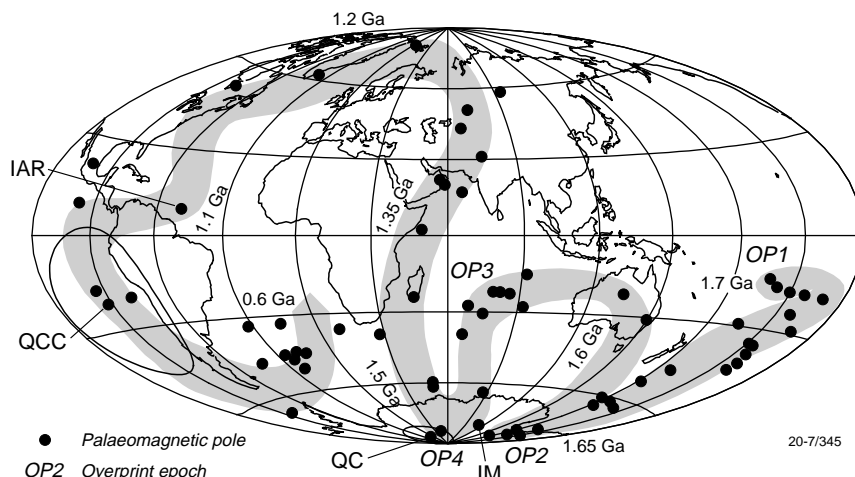
Fig. 7. 1700–600-Ma APWP for Australia (Idnurm et al. 1995: Precambrian Research, 72, 1–41) showing the pole QC for the Quamby Conglomerate in relation to the pole IM, which represents the last period of metamorphism in the Mount Isa Inlier. Also shown is the pole QCC from individual cobbles, which appears to represent a Grenvillean overprint, and the pole IAR from the Lakeview Dolerite and other coeval postmetamorphic dykes of the Mount Isa Inlier.

Secondly, the gold may be detrital, having been eroded from older rocks uplifted at ~1500 Ma and deposited on the beds of streams that followed the active faults. Recent petrological evidence seems to favour a detrital origin (Register of Australian Mining 1997/1998, Resource Information Unit, Subiaco, p. 194), but does not rule out a hydrothermal contribution.

A Grenvillean thermal event at Mount Isa?

The remanence component with the lower unblocking temperature in the slate cobbles appears to be a partial overprint superposed on either a primary magnetisation of the cobbles or some predepositional secondary magnetisation. Its absence from the arenite samples may be due to the high magnetic stability of the hematite in the arenite to heating. What caused the overprinting?

The pole QCC for the cobbles lies roughly on the same part of the APWP as the pole IAR for the postmetamorphic dykes of the Mount Isa Inlier (Fig. 7). These dykes include the 1100-Ma Lakeview Dolerite, which has been traced to within 35 km of the southernmost sampling site. The pole could thus represent either a thermal or a chemical overprint associated with the 1100-Ma

magmatism. The Mount Rosebee and Camel Creek Faults could have channelled heat or fluids to the Quamby Conglomerate. Temperature estimates based on theoretical calculations for pure magnetite (Middleton & Schmidt 1982: Journal of Geophysical Research, 87, 5351–5359), and a conservative unblocking temperature of ~500°C, suggest that a thermal overprint would have required a minimum temperature of 250°C for heating durations of 10 m.y. or less. Alternatively, secondary magnetite deposited from fluids that circulated at the time of the intrusion could be the source of a chemical overprint.

The magmatism may be part of the Grenvillean orogenesis, for which evidence has been sought in northeastern Australia.

Acknowledgment

[1] Minerals Division, Australian Geological Survey Organisation, GPO Box 378, Canberra, ACT 2601; tel. +61 2 6249 9314 (MI), +61 2 6249 9489 (LW); fax +61 2 6249 9972; e-mail midnurm@agso.gov.au, lwyborn@agso.gov.au.
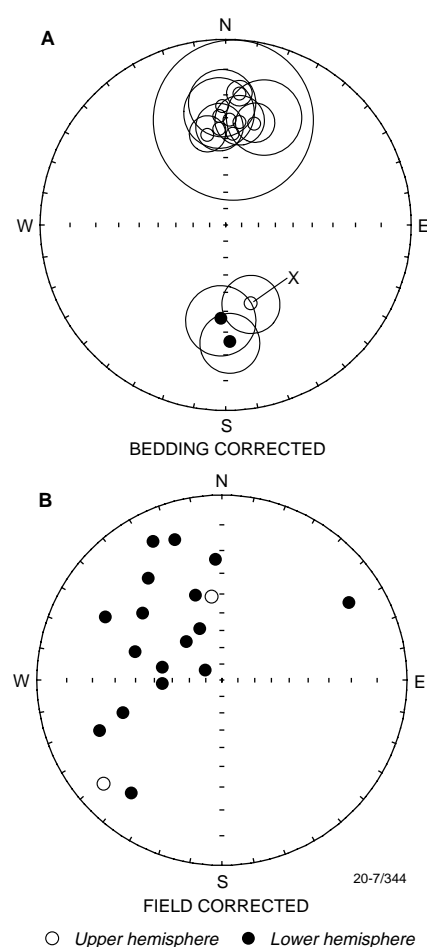

Fig. 6. Remanence directions of the Quamby Conglomerate: (A) Site mean directions and their 95% confidence circles in the arenites; the anomalous site mean direction is labelled X. (B) Overprint directions in the cobbles.

A comparison of Ordovician and Devonian magmatism in the eastern Lachlan Fold Belt: re-evaluating exploration targets

Ollie Raymond[1] & Shen-su Sun[1]

The importance of the role of Ordovician mafic to intermediate magmatism in the metallogenesis of the eastern Lachlan Fold Belt (LFB) has been increasingly recognised in the past decade. Ordovician igneous rocks host large gold and copper deposits of porphyry–epithermal style (e.g., North Parkes, Cadia, Peak Hill) and structurally controlled vein style (e.g., Sofala area), and are probable sources of metals in many younger deposits.

A commonly strong magnetic signature, 'shoshonitic' geochemistry, high platinum group element (PGE) concentrations, and strongly positive εNd isotopic signature have all been used in the past to characterise Ordovician magmatism (e.g., Wyborn 1988: BMR Research Newsletter, 8, 13–14; Wyborn 1992: Tectonophysics, 214, 177–192; Wyborn & Sun 1993: AGSO Research Newsletter, 19, 13–14). Recent sampling in the Dubbo and Forbes 1:250 000 Sheet areas (by AGSO and the NSW Department of Mineral Resources in association for the National Geoscience Mapping Accord, NGMA) has emphasised that characteristics of some Devonian volcanics, including possible source material, are remarkably similar to the Ordovician. As a consequence, the exploration potential of the Devonian should not be underestimated.

Nd-isotope systematics for Ordovician magmatic rocks

Ordovician volcanics and intrusives recently analysed for εNd (Fig. 8) include three samples from the Burranah Formation near Mudgee, two from the Tucklan Formation near Gulgong, and one monzonite from an intrusive complex in the Oakdale Formation at Comobella. All these analyses except one fall within or very close to the range of Ordovician igneous rocks (+5.7 to +8.0) defined by Wyborn & Sun (1993: op. cit.). The exception (+3.0) is from a hornblende basalt of the Tucklan Formation; though low, this value is still significantly higher than values obtained from Siluro-Devonian I- and S-type magmatic rocks in the LFB (0 to –10). This and another sample (from Gidginbung, south of West Wyalong; +4.2; Wyborn & Sun 1993: op. cit.) suggest that the lower limit of εNd values for Ordovician magmatism could be extended to +3.0.

The Cuga Burga Volcanics

The Lower Devonian Cuga Burga Volcanics are intermediate to mafic volcanics which crop out mainly in the Dubbo 1:250 000 Sheet area in two discontinuous belts (Fig. 1). The eastern belt, located along the Molong High, is structurally complex, but provides stratigraphic control for the age of the volcanics. The western belt occurs around the western and northern margins of the Lower

Devonian Yeoval granite complex. Included in this belt are the mafic volcanics hosting the Mount Aubrey gold deposit. Unlike the Middle Devonian A-type Dulladerry Volcanics, to which they were previously assigned (Lewis 1991: Minfo, 31, 6–7), these mafic volcanics do not exhibit A-type geochemical characteristics. Although stratigraphic control is lacking in the western belt, the volcanics appear to be comagmatic with more mafic phases of the Yeoval complex, which intrudes them (D. Wyborn, Australian National University, ANU, personal communication 1998).

Three samples of the Cuga Burga Volcanics were analysed for εNd (Fig. 8) — two from outcrops along the Molong High north of Orange and another (labelled Fairy Mount) on the eastern margin of the Narromine 1:250 000 Sheet area. The εNd values (+4.8 to +7.0) are within the range of Ordovician igneous rocks discussed earlier, and suggest that magmatism with a mantle-derived source was active during the early Devonian. The high εNd values may reflect a direct mantle source similar to the Ordovician magmatism (Wyborn 1992: op. cit.). Alternatively, mantle-like εNd values may be preserved during remelting of mantle-derived gabbroic material underplated to the lithosphere during Ordovician magmatism (Wyborn et al. 1987: Australian Journal of Earth Sciences, 34, 21–43).

Nd-isotope analyses of the Yeoval granite complex combined with Pb-isotope analyses may shed more light on the ability of the Nd-isotope method to indicate a primary mantle source. The Pb-isotope composition of Ordovician igneous rocks is similar to that of depleted mantle (Carr et al. 1995: Economic Geology, 1467–1505; Sun & Wyborn 1994:

Geological Society of Australia, Abstracts 37, 421). Magmas generated from a mixed source of Ordovician igneous rocks and a crustal component (such as LFB granites) have Pb-isotope compositions between depleted mantle and crustal Pb represented by the growth curve of LFB VMS deposits.

The Cuga Burga and Ordovician volcanics also have similar major- and trace-element geochemistry. Spidergrams of basaltic to andesitic rocks from the two units show a remarkable overlap (Fig. 9): both are generally calc-alkaline in character; they have low levels of the high-field-strength elements (HFSE) Ti, Nb, Zr, and Y, and moderately high levels of the large-ion-lithophile (LIL) elements Ba, Sr, and K. Figure 10 emphasises the similar TiO_2 contents of Cuga Burga and Ordovician basalts and andesites; TiO_2 levels below 1% have been considered in the past as virtually diagnostic of Ordovician mafic volcanics. A small group of Cuga Burga samples with considerably higher TiO_2 (1.5–2.5%) and other HFSE resembles other post-Ordovician intraplate volcanics in the eastern LFB. Most of these samples come from a thin discontinuous belt of volcanics between Nurea and Three Rivers in the Wellington 1:100 000 Sheet area. This group of Cuga Burga Volcanics has a different mantle source and/or petrographic origin.

Further similarities between Cuga Burga and Ordovician magmatic rocks are seen in the levels of Pt and Pd (Fig. 11). PGEs are typically more concentrated in Ordovician volcanics than similarly fractionated younger volcanics with similar silica contents (Wyborn 1990: BMR Research Newsletter, 13, 8). The similar PGE range in the Cuga Burga Volcanics suggests that similar magmatic processes, including sulphur-undersaturated
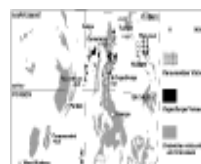

Click this image for a larger version
(73k)

Fig. 8. Sample localities for recent Nd-isotope studies of igneous rocks in the LFB NGMA mapping area, and their εNd values. The distribution of volcanic units is interpreted beneath cover rocks. For the locations of samples analysed for εNd, see Wyborn & Sun (1993: op. cit.).

NARROMINE

Dubbo

Tucklan +3.0

DUBBO

0   50 km

Comobella +7.0

+5.8

Burraneli
+5.7
+5.6
+6.2

Mudgee

33°00'

Fairy Mount
+5.6

+4.8 Cuga Burga
+7.0

FORBES

BATHURST

Parkes

Orange

Carawandool
+8.1

West Wyalong

148°30'

Carawandool Volcanics

Cuga Burga Volcanics

Ordovician volcanics
and intrusives
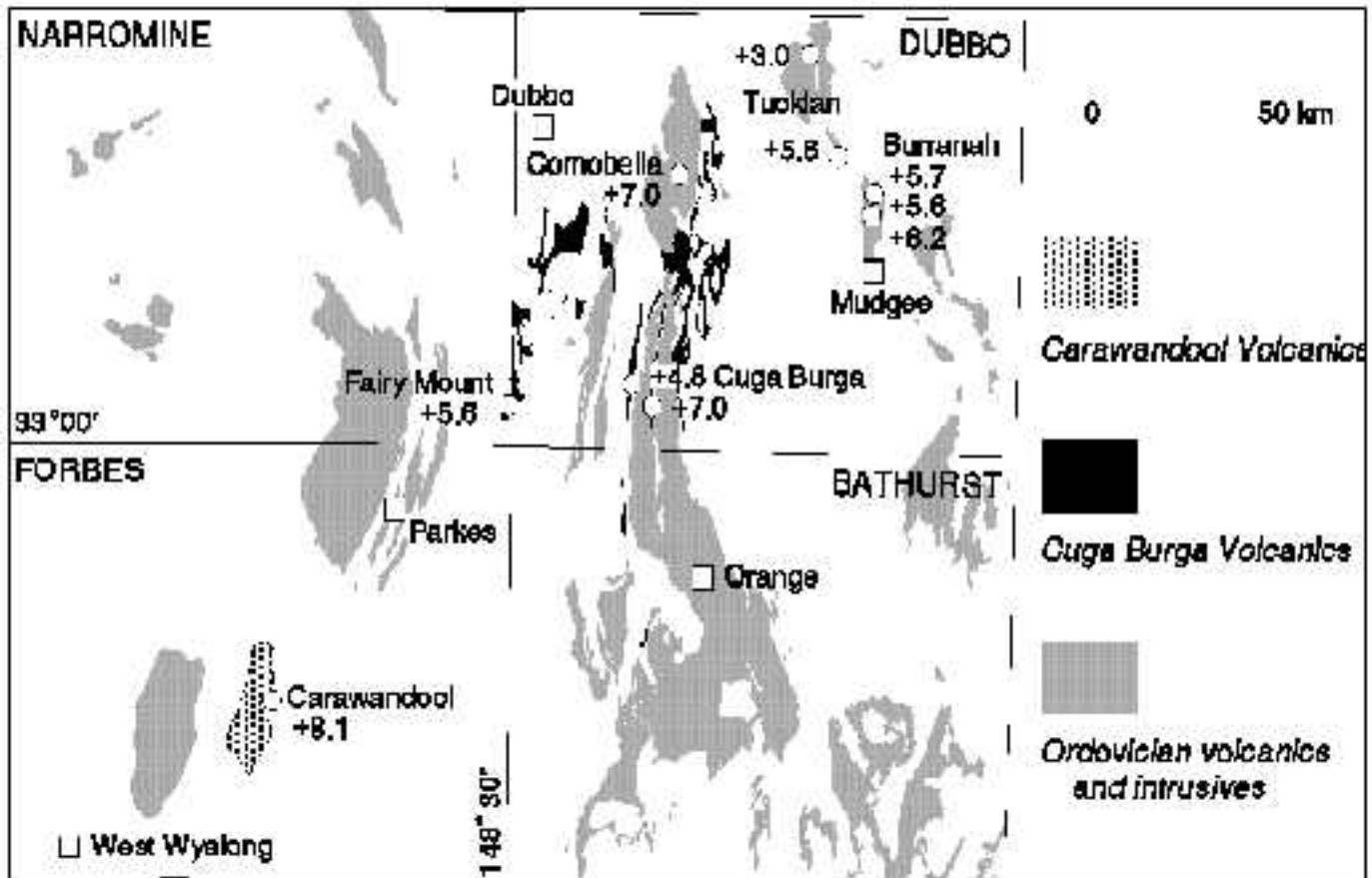
Fig. 9. Spidergram plot comparing basalts and andesites of the Lower Devonian Cuga Burga Volcanics with Ordovician igneous rocks of similar SiO$_2$ content (shaded area).
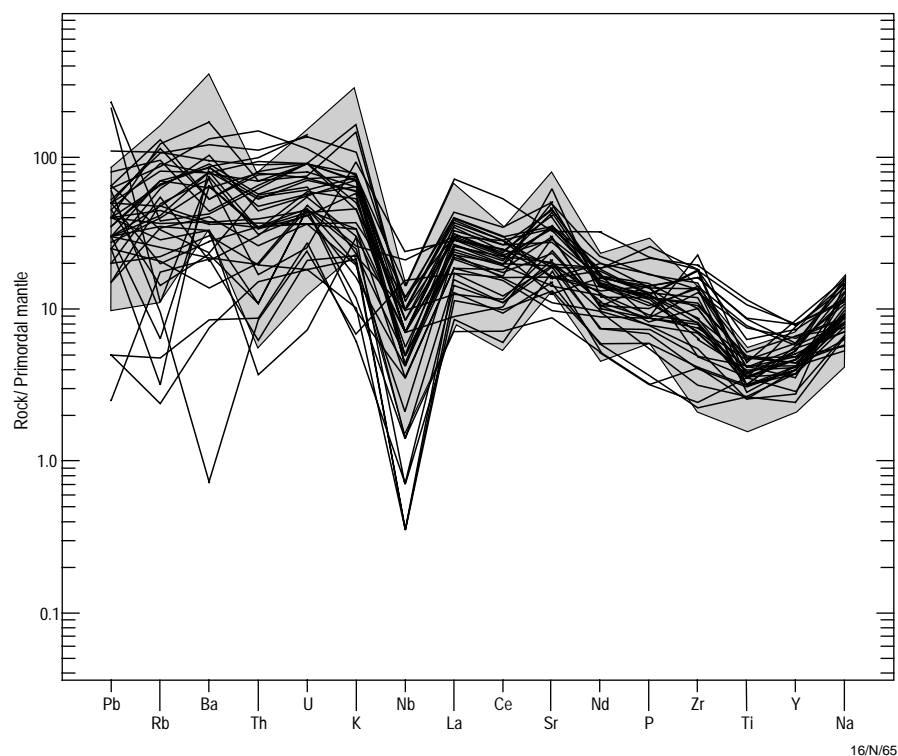
fractionation (Wyborn 1996: Minfo, 50, 4–6; McInnes 1997: Geological Society of Australia, Abstracts, 44, 49), also occurred in the Early Devonian.

The Carawandool Volcanics

The Carawandool Volcanics (incorporated as part of the Lower Devonian Milpose Volcanics by Bowman 1976: Forbes 1:250 000 metallogenic map, Geological Survey of New South Wales) form a broad syncline about 60 km southwest of Parkes (Fig. 8). They are primarily felsic volcanics with lesser basalts and andesitic lavas and breccias. NGMA mapping in 1997, and zircon U–Pb dating of the volcanics, have indicated an Early Devonian age (403.8 ± 2.1 Ma; L.P. Black, AGSO, personal communication 1998).

Regional magnetic response and εNd-isotope evidence had led researchers and explorers in recent years to regard the Carawandool Volcanics as Ordovician. Thin highly magnetic basalt layers in the largely felsic volcanic pile cause a strong magnetic response in regional magnetic surveys. This is similar to the strongly magnetic character of many Ordovician volcanics and has been used to interpret their distribution under cover. The linear magnetic anomalies due to the Carawandool basalts contrast strongly with the surrounding weakly magnetic rhyolites, and are much wider than the outcrop of the thin basalt flows. As a result, the strong magnetic signature of the volcanics seen on regional surveys is not particularly representative of the volcanics as a whole. Recent mapping of strongly magnetic rocks north of West Wyalong, also previously regarded as of Ordovician age, has shown that most are probably Silurian or Devonian. Many linear magnetic anomalies are structurally related rather than stratigraphic, emphasising the need to critically evaluate the interpreted distribution of Ordovician rocks based on regional magnetic response.

A single εNd-isotope analysis of a Carawandool Volcanics basalt returned a value of +8.1. Its strongly positive mantle-like character is similar to that of Ordovician magmatic rocks. Wyborn & Sun (1993: op. cit.) obtained an εNd value of +6.5 from a tourmaline-bearing hydrothermal breccia at Porters Mount associated with a buried intrusion on the southern edge of the Carawandool Volcanics. This result was assumed to indicate Ordovician-related mineralisation, and the Carawandool Volcanics, by analogy, were interpreted as Ordovician by later workers. However, analyses of the Cuga Burga Volcanics, discussed above, have shown that other geological features must be considered before an Ordovician age can be assumed. The εNd results appear to be reflecting a similar source for both Ordovician and Devonian magmatism.

The foregoing similarities between the Carawandool Volcanics and Ordovician Volcanics are not reflected in their major- and trace-element geochemistry. The Carawandool Volcanics have SiO$_2$ mostly above 65%; by contrast, from over 300 analyses of eastern LFB Ordovician igneous rocks in the AGSO/NSWDMR database, less
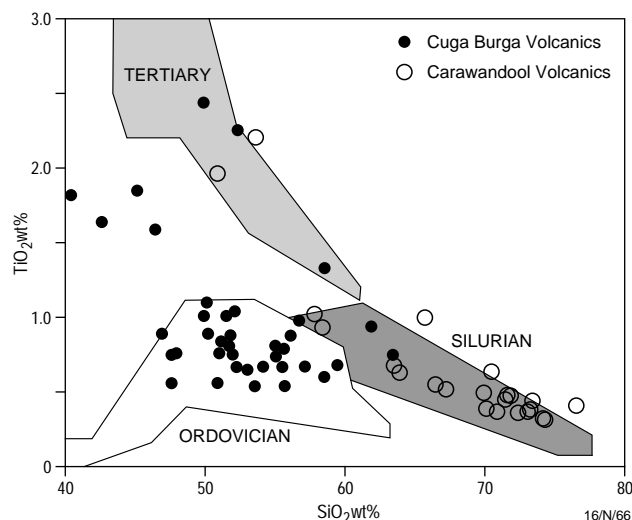

Fig. 10. Plot of TiO$_2$ vs SiO$_2$ comparing the Cuga Burga and Carawandool Volcanics with Ordovician, Silurian, and Tertiary igneous rocks from the eastern LFB.
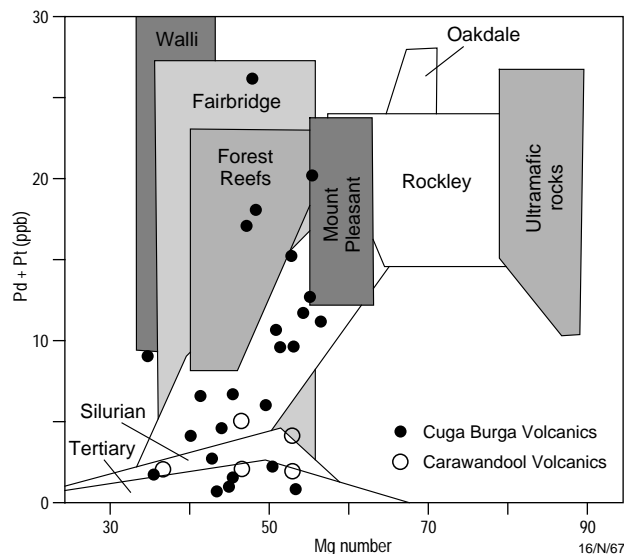

Fig. 11. Plot of (Pd + Pt) vs Mg number. Ordovician volcanics are from the Fairbridge, Forest Reefs, Mount Pleasant, Oakdale, Rockley, and Walli units, and from ultramafic rocks.

than 10 samples have SiO$_2$ greater than 62%, indicating the almost exclusively intermediate to ultramafic nature of Ordovician magmatism. Compared with Ordovician rocks of similar SiO$_2$ content, the Carawandool Volcanics have noticeably higher HFSE and show fractionation trends more akin to younger Palaeozoic and Cainozoic intraplate magmatic rocks in the LFB (Fig. 10). They also have generally lower levels of LIL elements and do not show calc-alkaline characteristics. The small amount of PGE data available for the mafic members of the Carawandool Volcanics shows low levels of Pt and Pd (Fig. 11) — a further contrast with the Ordovician volcanics.

Conclusions

Geochemical, isotopic, or magnetic evidence cannot be considered in isolation when interpreting the distribution and character of Ordovician magmatic rocks in the eastern LFB. Some previously applied discriminants of Ordovician magmatism may not be as robust as first thought, and several methods may have to be applied in concert. The sources and/or processes that contributed to the generation of magma during the Ordovician may have been duplicated during the Early Devonian, highlighting the economic potential of the Devonian in the eastern LFB.

[1] Minerals Division, Australian Geological Survey Organisation, GPO Box 378, Canberra, ACT, 2601; tel. +61 2 6249 9575 (OR), +61 2 6249 9484 (SS); fax +61 2 6249 9983; e-mail oraymond@agso.gov.au, ssun@agso.gov.au.

AGSO's new confocal laser Raman microprobe

Terrence P. Mernagh[1]

AGSO recently acquired a state-of-the-art laser Raman microprobe (Fig. 12), which is the first one of its kind in Australia. New features such as 3D confocal imaging and Raman mineral mapping increase the capabilities of AGSO's national Raman microprobe facility, and provide important information on a much wider range of geological materials. The Raman microprobe's three laser wavelengths, broad detector range (from the visible to the near-IR), and high confocal resolution (down to 1 μm) enhance the study of fluid inclusions (in both ore deposits and petroleum reservoirs), and the identification of individual minerals in hand specimens, drillcores, and thin sections. The line-scanning accessory facilitates the generation of Raman mineral maps of drillcore or thin sections. Both the Raman data and images of the samples can be digitally captured and stored in corporate databases.

The Dilor SuperLABRAM (Fig. 12) has two interchangeable holographic gratings and a liquid-nitrogen-cooled, 2000 x 800-pixel, charge-coupled detector to provide high sensitivity. Samples are analysed on a confocal petrological microscope equipped with oculars, a video camera, a macro device (for larger samples), and — to facilitate automated Raman mineral mapping — a confocal line scanner, motorised XY stage, and autofocus. An optical-fibre probe can be directly attached to the Raman's spectrometer to obtain spectra from remote or large objects. The samples can be probed by a range of laser wavelengths — including 514.5 nm (argon ion laser), 633 nm (HeNe laser), and 785 nm (near-IR diode laser) — which are needed for different applications (see below). The spectrometer and microscope are fully computer-controlled by Windows-compatible software which acquires the Raman data, captures the video images, and performs many arithmetic operations — including 3D manipulations of the spectra.
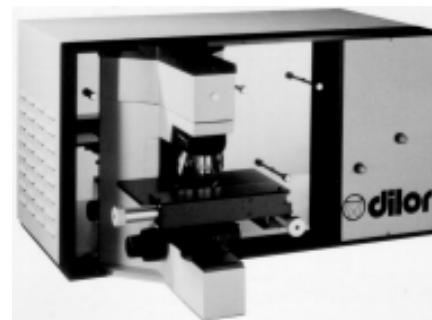

Fig. 12. AGSO's new SuperLABRAM Raman spectrometer with confocal microscope.

data can be used to determine other thermodynamic parameters (e.g., pH, fO_2, etc.; Dubessy et al. 1992: European Journal of Mineralogy, 4, 885–894).

Until now, calculating the absolute concentration of species in fluid inclusions was difficult owing to the irregular shape of many inclusions and the associated problems of accurately determining the volume. The
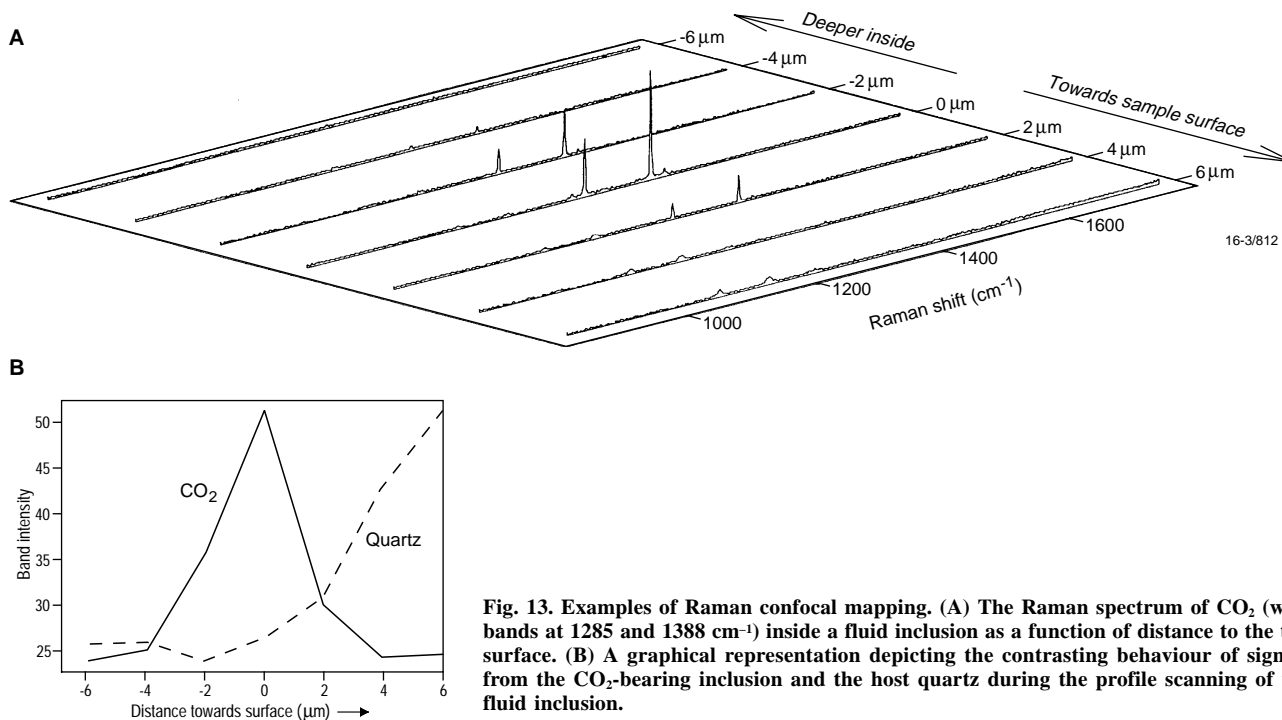

Fig. 13. Examples of Raman confocal mapping. (A) The Raman spectrum of CO_2 (with bands at 1285 and 1388 cm⁻¹) inside a fluid inclusion as a function of distance to the top surface. (B) A graphical representation depicting the contrasting behaviour of signals from the CO_2-bearing inclusion and the host quartz during the profile scanning of the fluid inclusion.

The Raman effect involves the interaction of light with matter, causing the emission of wavelengths of light with energies corresponding to a sample's molecular vibrations. This results in a unique Raman fingerprint for each compound. Raman spectra can be obtained from solids, liquids, and gases, and from both crystalline and amorphous compounds. This technique offers the following advantages:

- non-destructive analysis in air with little or no sample preparation,
- high spatial resolution (³1 μm), and
- sample analysis at high and low temperatures or pressures.

Fluid-inclusion studies

The laser Raman microprobe has been used to obtain important data on the composition of fluid inclusions ever since it was first invented (Rosasco et al. 1975: Science, 190, 557–560); now, fluid-inclusion studies are commonly considered incomplete if they lack these data. The Raman microprobe is particularly useful for the analysis of gases (e.g., CO_2, N_2, H_2S, CH_4, etc.) and solid phases in the inclusions (Dubessy et al. 1989: European Journal of Mineralogy, 1, 517–534). In addition, it can identify various dissolved polyatomic species, from which the

subtle changes in refractive index between the host rock and inclusion make it difficult to determine the volume of the inclusion because optical microscopes can focus only on the waist of the inclusion. However, equipping the spectrometer with a confocal microscope with a vertical resolution of around 1–2 μm enables the microprobe to carry out a series of depth scans, from which the spectra generated define the vertical dimensions of an inclusion (Fig. 13). A similar series of lateral scans at each depth interval completely defines the shape of an inclusion. This not only assists the Raman studies but enormously

benefits other microanalytical techniques, such as PIXE, which need precise information about the shape and volume of an inclusion in order to compensate for the effects of X-ray absorption (Ryan et al. 1995: Instruments & Methods in Physics, Research Section B — Beam Interactions, Materials & Atoms, 104, 182–190).

Hydrocarbon fluids and gases

Economic and environmental considerations have fuelled a growing interest in the study of free-moving fluids and gases (i.e., petroleum, natural gas, and water) in sediments. Hydrocarbon-bearing inclusions are commonly identified by the fluorescence they emit when illuminated by visible or UV light. This tendency to fluoresce has previously made it difficult to obtain Raman spectra from hydrocarbon-bearing samples. Now, however, this problem can be largely overcome by using the near-IR diode laser, which emits at a wavelength of 785 nm. Thus, the SuperLABRAM can assist the study of hydrocarbon migration by rapidly identifying organic tracers trapped in rocks or fluid inclusions. The CH_3/CH_2 ratios obtained from the Raman microprobe spectra can be used as a maturation index (Pironon 1993: Comptes Rendes Academie des Sciences, 316, Serie II, 1075–1082), and organic coatings on minerals can be studied to establish the time relationships between fracture-porosity formation and oil migration.

Mineral and alteration mapping

The benefits of using the laser Raman microprobe to identify minerals in thin section, rock chips, and drillcore have been previously described in detail (Mernagh et al. 1996: AGSO Research Newsletter, 25, 14–16). The confocal imaging capabilities of the SuperLABRAM make it highly suitable for identifying very fine-grained mixtures of minerals, such as those commonly encountered in alteration zones surrounding
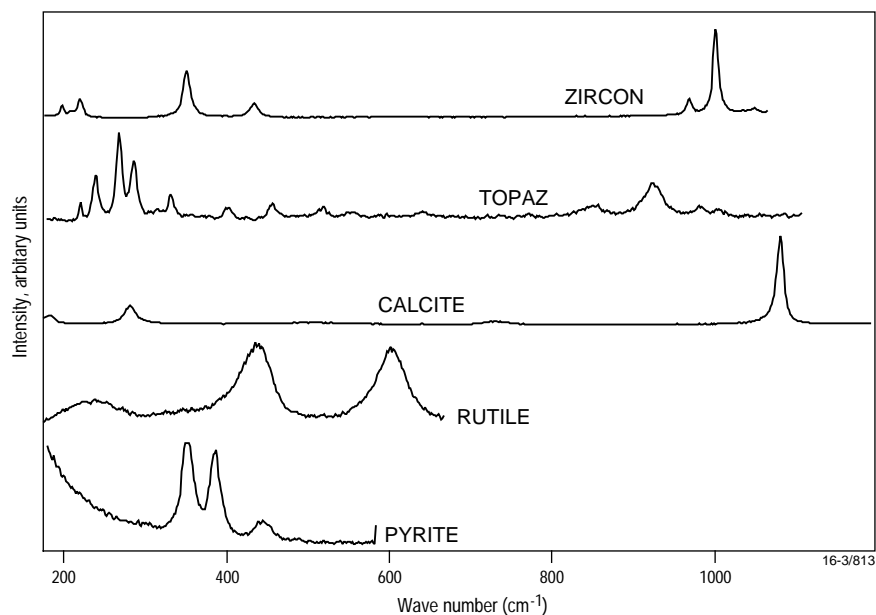

Fig. 14. Examples of Raman spectra of selected minerals.

hydrothermal mineral deposits. Note that the Raman microprobe can identify a wide range of minerals — including most silicates, carbonates, sulphates, nitrates, phosphates, hydroxides, oxides, and sulphides.

The confocal line-scanning attachment converts the laser beam from a single point into a line that can vary in length from a few micrometres to a few millimetres. Used in conjunction with the motorised XY stage, it can scan the length of a section of drillcore or a thin section. This produces a Raman map of the sample, from which the various minerals can be identified by observing the frequencies of the bands within the spectra (Fig. 14). As the data are all digitally captured, they can be further processed to reveal the percentage abundance of each mineral, or other types of information. Furthermore, these maps and spectra can be stored in corporate databases linked with other petrological or geochemical information.

The new laser Raman microprobe will contribute important geochemical and mineralogical data to a wide range of AGSO's projects. The foregoing examples illustrate just a few of the many possible applications of the SuperLABRAM. The instrument will continue to operate as a national research facility, and researchers from industry and academia are invited to use it for collaborative studies or on a commercial basis.

Please contact the author for more information.

[1] Minerals Division, Australian Geological Survey Organisation, GPO Box 378, Canberra, ACT 2601; tel. +61 2 6249 9640; fax +61 2 6249 9983; e-mail tmernagh@agso.gov.au.

Problems with the Cretaceous biostratigraphic system of Australia: time for a review

Samir Shafik[1]

Most users of biostratigraphic results, including those based on Cretaceous sequences, assume that the biozonation applied is without serious problems, represents a time continuum, and has been firmly linked (at least partly) to standard timescales and other biozonations. However, problems in the biostratigraphic system of the Australian Cretaceous abound. They are particularly evident where, for instance:

- **acme zones are used (e.g., the Early Cretaceous dinoflagellate *Ascodinium cinctum* Zone),**
- **a zonal boundary is defined by multiple bioevents (some of the foraminiferal C zones; see below), or**
- **bioevents are based on species from different biogeographic provinces (e.g., the nannofossils *Monomarginatus quaternarius* and *Quadrum trifidum* in the Campanian of the Perth and Carnarvon Basins respectively).**

These problems usually cause doubtful biostratigraphic assignment or imprecise correlation. Imposed on these problems is the widespread practice in oil exploration of applying informal zones whose definitions have not been published (e.g., the nannofossil KCN zones), and which therefore are not available for correlation with published zones inside and outside Australia.

Because of the demand from several disciplines (e.g., seismic stratigraphy, geological modelling, etc.), numerical ages have been assigned to Cretaceous zonal boundaries in Australia, even though links with the standard numerical timescale are commonly tenuous at best. This practice of assigning numerical ages to biostratigraphic events, although necessary, is potentially dangerous if it is allowed to mask any of the biostratigraphic problems or to render unnecessary the efforts of identifying biozonal anchor points to the standard numerical timescale. A summary of the biochronology of the Australian Cretaceous was published in the AGSO-inspired monograph 'An Australian Phanerozoic timescale' (1996: Oxford University Press), which serves as a focus for more detailed work.

A review of the Australian Cretaceous biostratigraphic system and its links with published timescales is overdue, and is being undertaken as part of AGSO's 'Timescale calibration and development' project. All relevant fossil groups are targeted in the review, primarily:

- to identify any anchor points of their zones to the standard numerical timescale,
- to diagnose points of weakness in the Australian Cretaceous biostratigraphic system as a whole, and
- to implement ways of rectifying them.

Discussion

The ages of many local Late Cretaceous dinocyst zones (see Helby et al. 1987: Association of Australian Palaeontologists, Memoir 4, 1–94), particularly in northwest Australia, have been derived from the largely unpublished, local calcareous planktic biostratigraphy. Original data linking the two biostratigraphies are mostly unpublished, and the nannofossil or foraminiferal schemes to which Helby et al. referred were in the process of being developed. For example, the late Campanian age for the *Isabelidinium korojonense* Zone (Helby et al. 1987: op. cit., fig. 32) is based on foraminiferal data in the

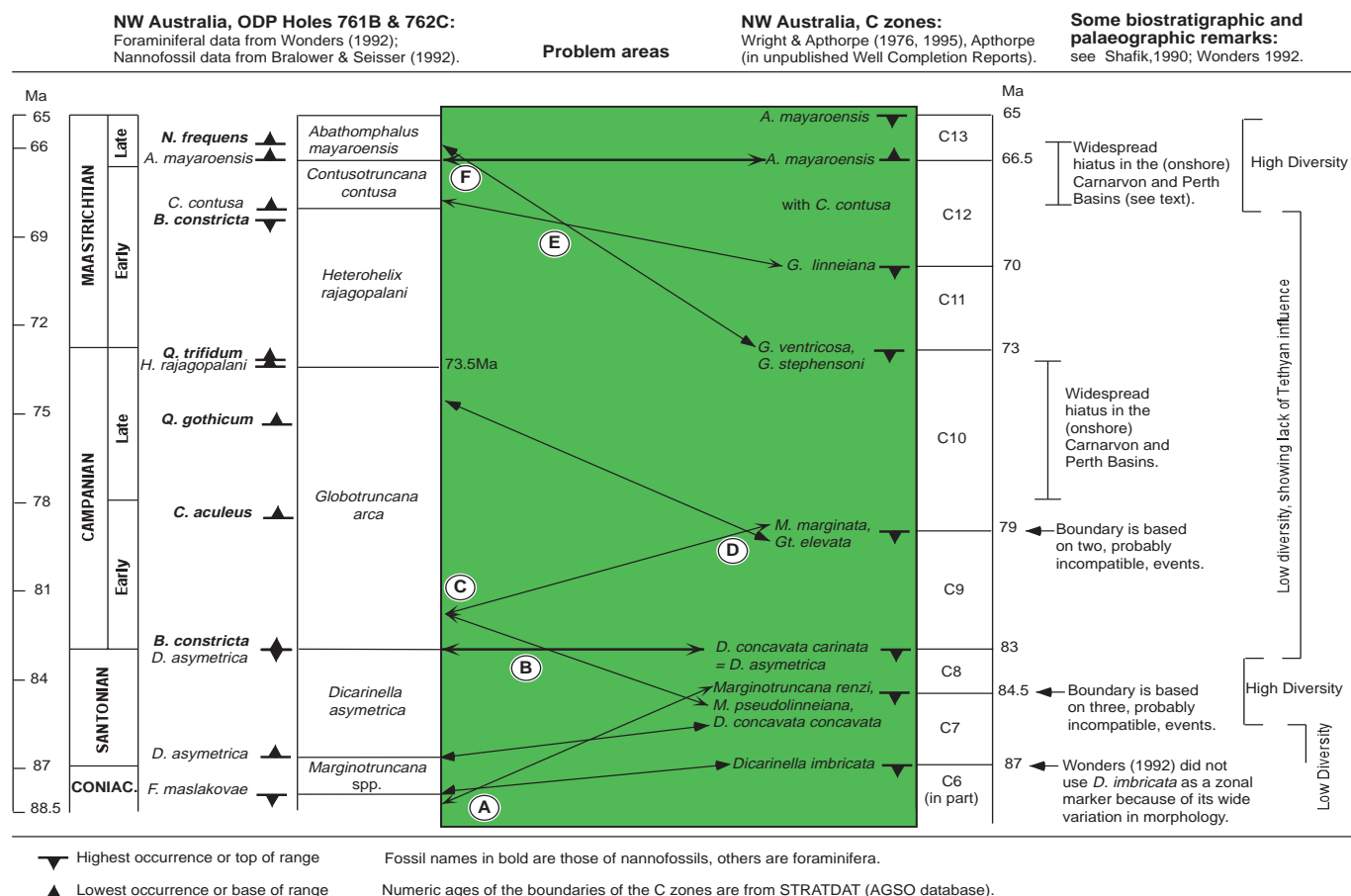| NW Australia, ODP Holes 761B & 762C:
Foraminiferal data from Wonders (1992);
Nannofossil data from Bralower & Seisser (1992). | Problem areas | NW Australia, C zones:
Wright & Apthorpe (1976, 1995), Apthorpe
(in unpublished Well Completion Reports). | Some biostratigraphic and
palaeographic remarks:
see Shafik,1990; Wonders 1992. |

Fig. 15. Apparent problems with the C zones in northwest Australia, as indicated by data from ODP sites 761 (Wombat Plateau) and 762 (Exmouth Plateau). The tops of the ranges of key C zone species in ODP drillholes 761B and 762C are based on data in Wonders (1992: *in* von Rad et al. op. cit., 587–599). The tops of species ranges are taken at the highest occurrences of the same species in Wonders's (1992: op. cit.) charts — regardless of their abundance below this level. Bibliographic details of other cited references are annotated in the text.

unpublished well completion reports for Esso Zeewulf No. 1 and Houtman No. 1, and on foraminiferal and nannofossil data in an unpublished thesis. It is now time to review and update these data.

Similarly, a host of problems (graphically portrayed in Fig. 15) foreshadow the need to review the status of most of the local foraminiferal C zones of Wright (1973: BOC Australia Ltd, unpublished report), Wright & Apthorpe (1976: Journal of Foraminiferal Research, 6, 228–240), and Wright & Apthorpe (1995: Second International Symposium on Cretaceous Stage Boundaries, Brussels, 8–16 September, 1995, abstract volume, 28). These zones were developed for northwest Australia, and can be readily tested against the data acquired from the continuously cored sites on ODP Leg 122 off northwest Australia (von Rad et al. 1992: Proceedings of the Ocean Drilling Program, Scientific Results, 122; College Station, Texas).

North West Shelf examples

The problems illustrated graphically in Figure 15 include:

A. In hole 762C, *Dicarinella imbricata*, the top of which defines the top of zone C6, ranges consistently above the top of *Marginotruncana renzi*, which defines the top of zone C7. Equally important, *M. renzi, M. pseudolinneiana,* and *Dicarinella concavata concavata*, whose tops define the top of zone C7, disappear upsection in 762C at different levels: the top of *M. renzi* is well below the top of *M. pseudolinneiana*, and the top of *D. concavata concavata* is in between.

B. In hole 762C, the top of *Marginotruncana pseudolinneiana* (= top of zone C7) is above the top of *Dicarinella asymetrica* (= top of zone C8). In hole 761B, both *D. asymetrica* and *M. pseudolinneiana* disappear upsection at the same level.

C. Interval C8–C9, from the top of *Marginotruncana pseudolinneiana* (top of zone C7) to the top of *M. marginata* (top of zone C9), is questionable: in hole 762C, the two species disappear upsection at the same level, the former having a consistent range and a better top.

D. Placing the top of zone C9, at the tops of *Marginotruncana marginata* and *Globotruncanita elevata*, introduces a possible inconsistency: in hole 762C, *M. marginata* disappears well below the top of *Gt. elevata*.

E. In both 761B and 762C, *Globotruncana ventricosa* (the top of its range = top of zone C10) ranges above the top of *G. linneiana* (= top of zone C11).

F. Interval C11–C12 is questionable: the two defining species *Gobotruncana*

ventricosa (the top of its range = top of zone C10) and *Abathomphalus mayaroensis* (the base of its range = base of zone C13) overlap in holes 761B and 762C. The overlap in the ranges of *G. ventricosa* and *A. mayaroensis* is very short in 762C (because of a perceived unconformity in this hole at the base of the *A. mayroensis* Zone — discussed below), but longer in 761B, where there is no unconformity. *Globotruncana ventricosa* may not be considered reworked because it ranges to near the top of the Maastrichtian (see, e.g., Caron 1985: Cambridge Earth Science Series, Cambridge University Press, Cambridge).

The foregoing problems cannot be ignored because it is only through correlation networks that the temporal sequence of bioevents can be established — a preliminary basic step to biostratigraphy. Diachronism of bioevents is well documented, but probably cannot be used as an explanation here, because we are dealing with only a narrow range of latitude — northwest Australia during the Late Cretaceous.

Data based on core material, especially from continuously cored sites (as in ODP holes 761B and 762C), undoubtedly rank higher in the scale of confidence/reliability than those based on ditch cuttings, spot cores, or side-wall cores (as is usually the case in oil exploration) — the basis for the C zones.

In evaluating foraminiferal data from well-completion reports for input to its STRATDAT database, AGSO has preferred to use the zonation of Caron (1985: op. cit.), rather than the C zones, which currently remain mostly unpublished. Even so, the zonation of Wonders (1992: *in* von Rad et al. op. cit., 587–599), although not without problems, is better suited for northwest Australia. Nevertheless, for a precise correlation with sections outside northwest Australia, a thorough knowledge of the local stratigraphic ranges is vital. For example, does the reduced range of *Contusotruncana contusa* in northwest Australia reflect a late arrival of the species (Wonders 1992: op. cit.) or unconformity (Apthorpe 1979: APEA Journal, 19, 74–89)?

A review of the Australian Cretaceous biostratigraphic system will necessitate a rigorous interpretation of biostratigraphic data and an understanding of the local stratigraphy. For example, in a reinterpretation of published biostratigraphic data (Fig. 16), the distribution of both foraminifera and nannofossils in the Campanian–Maastrichtian section of hole 762C on the Exmouth Plateau differs from that in hole 761B on the Wombat Plateau — with two important consequences:

- On the Exmouth Plateau, the key foraminifer *Abathomphalus intermedius* is absent; there is no overlap between the nannofossil *Reinhardtites levis* and the

foraminifer *Abathomphalus mayaroensis*; and the tops of *R. levis* and *Broinsonia constricta* coincide — in sharp contrast with the record from the Wombat Plateau. I interpret these observations as indicating an intra-Maastrichtian hiatus on the Exmouth Plateau, in hole 762C. This hiatus was not recognised by von Rad et al. (1992: op. cit.), even though they did not record the mid-Maastrichtian *Contusotruncana contusa* Zone at site 762.

- The thickness of the preserved zones in hole 762C is two to five times that of the corresponding zones in hole 761B, indicating much slower sedimentation rates in hole 761B, where — ironically — the mid-Maastrichtian *Contusotruncana contusa* Zone *is* present. Thus, the Maastrichtian section in hole 761B is *condensed* but *more complete*, whereas in hole 762B the section is *expanded* by comparison and includes a *hiatus*.

Evidence elsewhere suggests that the intra-Maastrichtian hiatus is widespread in northwest Australia. I have described a coeval unconformity in both the onshore Carnarvon and Perth Basins (Shafik 1990: BMR/AGSO Report 295), and Apthorpe (1979: op. cit.) has recorded a similar unconformity in offshore northwest Australia.

Identification of hiatuses and accurate determination of sedimentation rates in a sedimentary sequence are among the most significant elements in its geological interpretation. These cannot be achieved without good biostratigraphic schemes firmly anchored to a calibrated numerical timescale.

A southeast Australian example

In the Otway Basin of southeast Australia, most of the formational boundaries in the Cretaceous Sherbrook Group coincide with (sub)zonal boundaries (spore and pollen, and dinocysts; Fig. 17). This scheme may be faultless, but it does raise a few questions:
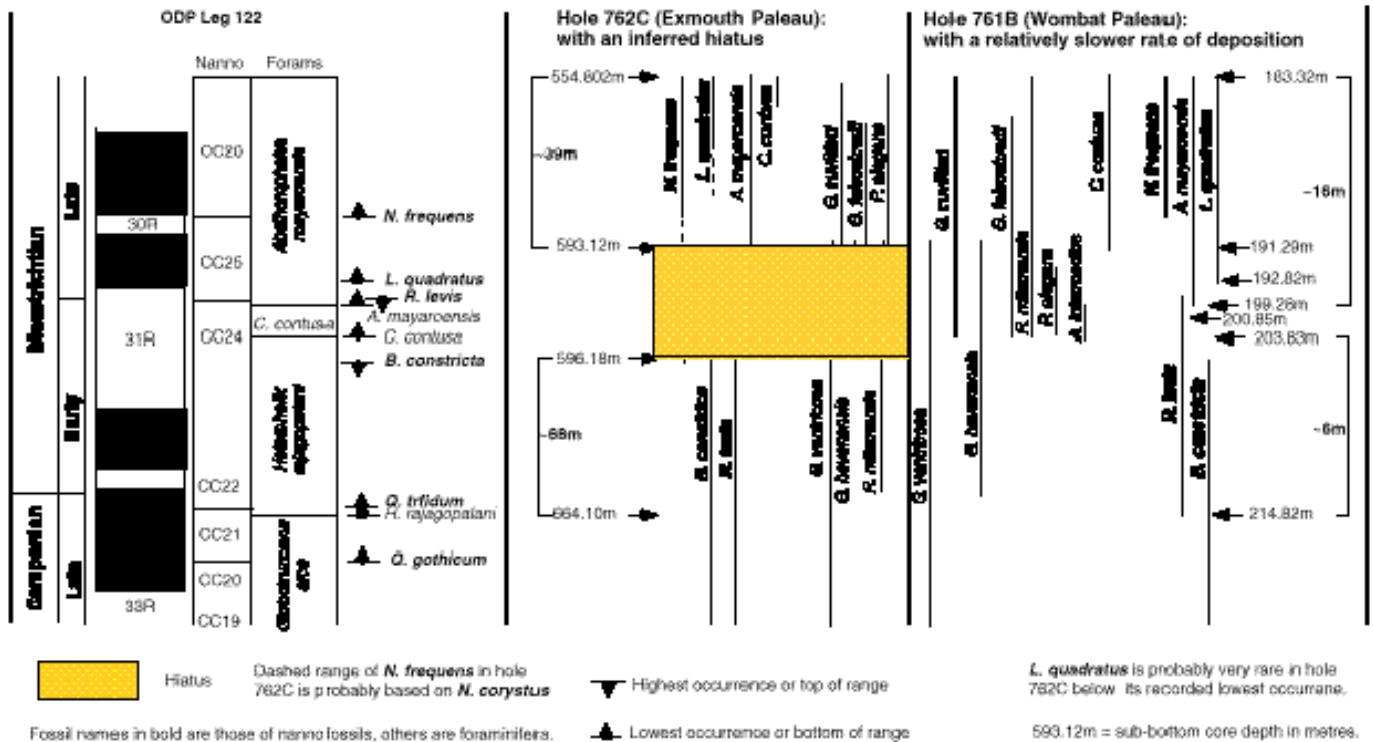
- Such a coincidence of formational and (sub)zonal boundaries usually suggests that the (sub)zones are controlled by facies. Are they here? The answer is probably no, because the geographic distribution of the zones seems very wide in the marginal basins of both southeast and northeast Australia.

- Also, does the coincidence of formational and (sub)zonal boundaries suggest intraformational unconformities? A 'yes' answer cannot be ruled out in some instances, but would be difficult to prove, unless sections containing other groups of microfossils (e.g., the combination of palynomorphs, foraminifera, and nannofossils) are found. The assumption that a zonation represents a time continuum may then be challenged.
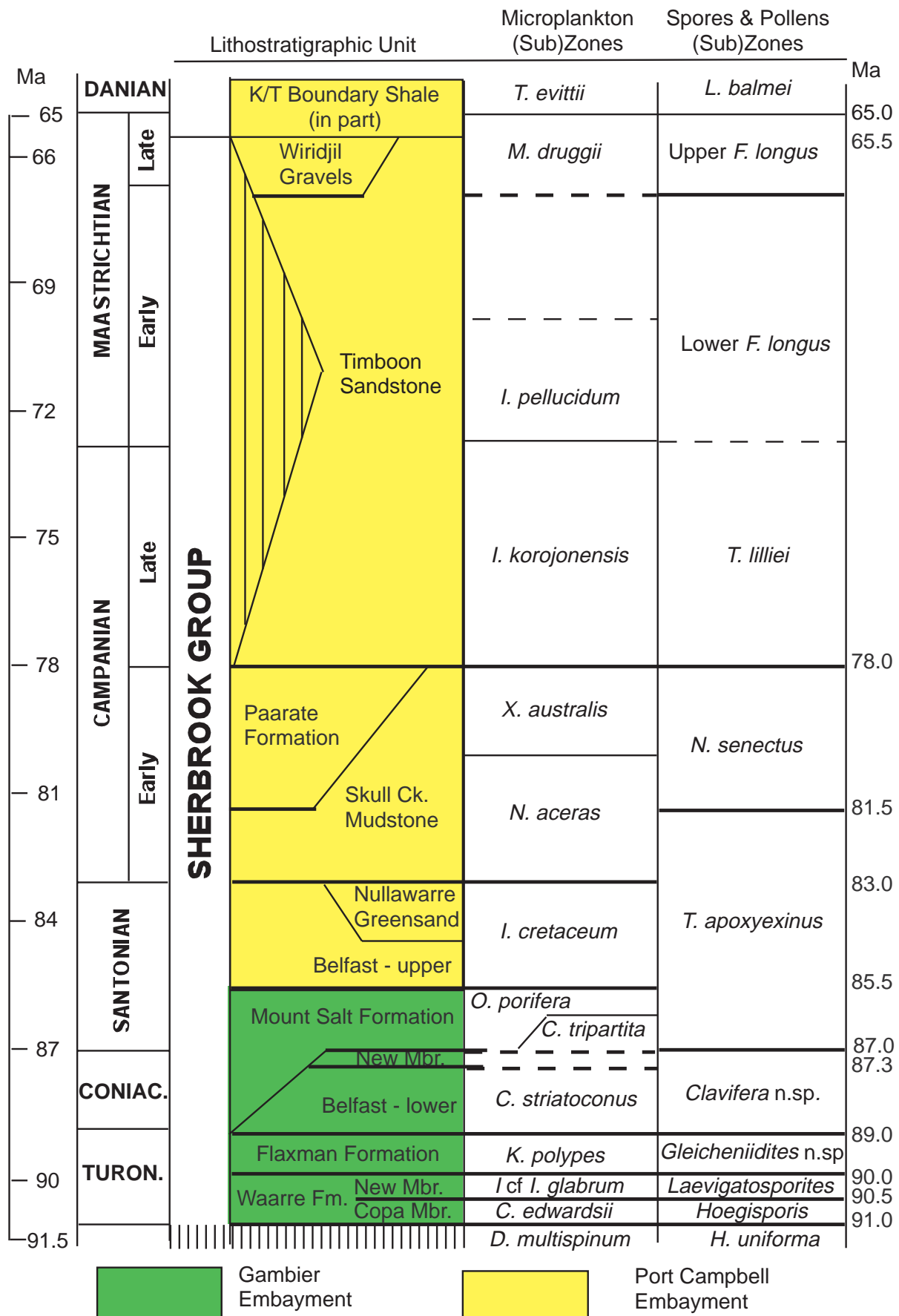
Conclusion

The Australian Cretaceous biostratigraphic system is riddled with problems, which demonstrate the need for it to be reviewed and its basis updated. Identifying its anchor points to standard timescales is also a priority in recognition of the great importance of characterising sedimentary sections — e.g., defining hiatuses and estimating sedimentation rates — as precisely as possible.

[1] Petroleum & Marine Division, Australian Geological Survey Organisation, GPO Box 378, Canberra, ACT 2601; tel. +61 2 6249 9436; fax +61 2 6249 9986; e-mail sshafik@agso.gov.au.

Fig. 16. Reinterpreted nannofossil and planktic foraminiferal biostratigraphy of the Campanian–Maastrichtian of ODP holes 762C and 761B (biostratigraphic data from Wonders 1992: op. cit; and Bralower & Seisser 1992: *in* von Rad et al. op. cit., 529–556; palaeomagnetic data from Galbrun (1992: *in* von Rad et al. op. cit., 699–716).

Fig. 17. Biostratigraphy of the Sherbrook Group in the Otway Basin (after Partridge 1997: PESA News, April/May, p. 9). Lines representing coinciding zonal and formational boundaries are thickened.

Gamma-ray spectrometric data: modelling to map primary lithology and later chemical mobilisation

Peter Wellman[1]

Whereas the accuracy and detail of gamma-ray spectrometric surveys have improved during the last 10 years, techniques for analysing the geological significance of the absolute abundances of K, Th, and U in the acquired data have not. Commonly the final product is a single image showing the concentrations of K, Th, and U as the intensity of red, green, and blue (RGB). This colour image is qualitatively interpreted either by mapping areas of the same perceived colour, or by classifying (either supervised or unsupervised) the K–Th–U space according to pixel concentrations. Both interpretation techniques largely express distances along the path of the average geochemical variation of the data. Differences from this average variation are poorly expressed, although this is often the main interest to the interpreter.

Modelling the K–Th–U data

For major rock groups, the K–Th–U data correlate with one another. Analysing the data in terms of their geological significance depends on choosing other nearly orthogonal axes in K–Th–U space, such that:

* components along the new axes are largely uncorrelated;
* the new axes have meanings with respect to geological processes; and
* the data analysis is preferentially based on the elements measured with the greatest accuracy relative to their abundance range.

The interpretation method advocated herein considers four major groups of rock separately — sedimentary rocks, and felsic, intermediate, and mafic igneous rocks. For each of these groups, variation diagrams (scattergrams) are plotted to show the distribution of pixels in the planes K–Th, K–U, and Th–U. Importantly, the diagrams show a concentration of points along the line of average geochemical variation in K–Th–U space. The first component is the distance along the path of average geochemical variation. Other components are best defined as the anomalous concentration of other elements with respect to this average variation.

If the objective of the interpretation is to define original lithology to aid the construction of a geological map, the images are made generally to emphasise the variation in the first component — i.e., with many subdivisions along the line of average geochemical evolution, and fewer subdivisions in the direction of other components.

If the objective of the interpretation is to identify areas and types of subsequent change in geochemistry, the interpretation strategy depends on the rock group and its history. One strategy is to model the average geochemical variation of the rock group, and separate and map all pixels with compositions that differ significantly from this model. Another strategy is to map the variation in an element that is independent of primary lithological layering (e.g., U in some mafic igneous rocks), and may indicate a process such as hydrothermal alteration.

The components of the data can be displayed as:

* a single component shown as an intensity image;
* three components shown as an RGB image; or
* a geochemical map produced by dividing components into classification layers, and dividing the area into groups of pixels or into polygons.

In modelling spectrometric data, some experimentation is required to determine the optimal size area for a rock group to be geochemically modelled. Useful results can be obtained by modelling an area the size and complexity of the north Pilbara Craton. However, there are real differences in geochemical evolution between some batholiths, and between some mafic igneous sequences. Modelling is more informative if restricted to a rock group with a single well-defined evolutionary path.

Examples of the method

The following examples relate to a gamma-ray spectrometric dataset of the Marble Bar 1:250 000 Sheet area, which mainly comprises exposed Archaean rocks of the north Pilbara Craton. AGSO surveyed this area along flight lines 400 m apart at an altitude of 80 m above ground level. The data have not been improved by analysing all 256 channels to improve counting statistics, nor have they been downward-continued to ground level.

For intrusive felsic rocks (Fig. 18), the amount of geochemical evolution is difficult to quantify in the traditional display (Fig. 18a), in which the differences from the mean geochemical evolutionary path are seen only for rocks having elements with intermediate concentrations. In displays of the modelled data (Fig. 18b & c), the distance along the geochemical evolutionary path, and differences from the path, are visualised separately. Both batholiths depicted in Figure 18b and c are composed of a mosaic of different plutons that differ in their Th and U contents. Whereas the amount of evolution in the Corunna Downs Batholith (in the northeast) increases systematically to the southeast, the Shaw Batholith (in the west) displays no such systematic evolutionary trend.

Analysis of spectrometric data of the mafic flows is complicated by flows being thinner than the pixel size, by adjacent flows commonly differing in composition, by the presence of sedimentary and other volcanic rocks intercalated with the flows, by the terrain effects of float material near strike-ridges, and by the larger analytical errors due to moderately low concentrations of K, Th, and U. For the mafic volcanics of the Coongan Syncline, the deficiencies of a traditional RGB display of K–Th–U data (Fig. 19a) are apparent in a comparison with displays of modelled data (Fig. 19b–d). A measure of geochemical evolution (Fig. 19b) shows significant differences across strike both regionally and locally. Anomalous Th (Fig. 19c) shows that the mafic sequences have characteristic mean Th differences from the mean geochemical evolutionary path. Anomalous U (Fig. 19d) is a measure of geochemical mobilisation, and the high and low values may reflect the location of hydrothermal systems. This figure highlights the area of anomalously high U in the northeast. Note the increasing image degradation from Figure 19b–d owing to low spectrometer count rates over areas of low concentration of Th and U.

The above examples show the power of displaying the spectrometric data analyses with respect to the average geochemical evolutionary path. The data and displays should be useful for analysing geochemical evolution, for lithological mapping, and for identifying areas of subsequent geochemical change.

[1] Minerals Division, Australian Geological Survey Organisation, GPO Box 378, Canberra, ACT 2601; tel. +61 2 6249 9653; fax +61 2 6249 9983; e-mail pwellman@agso.gov.au.
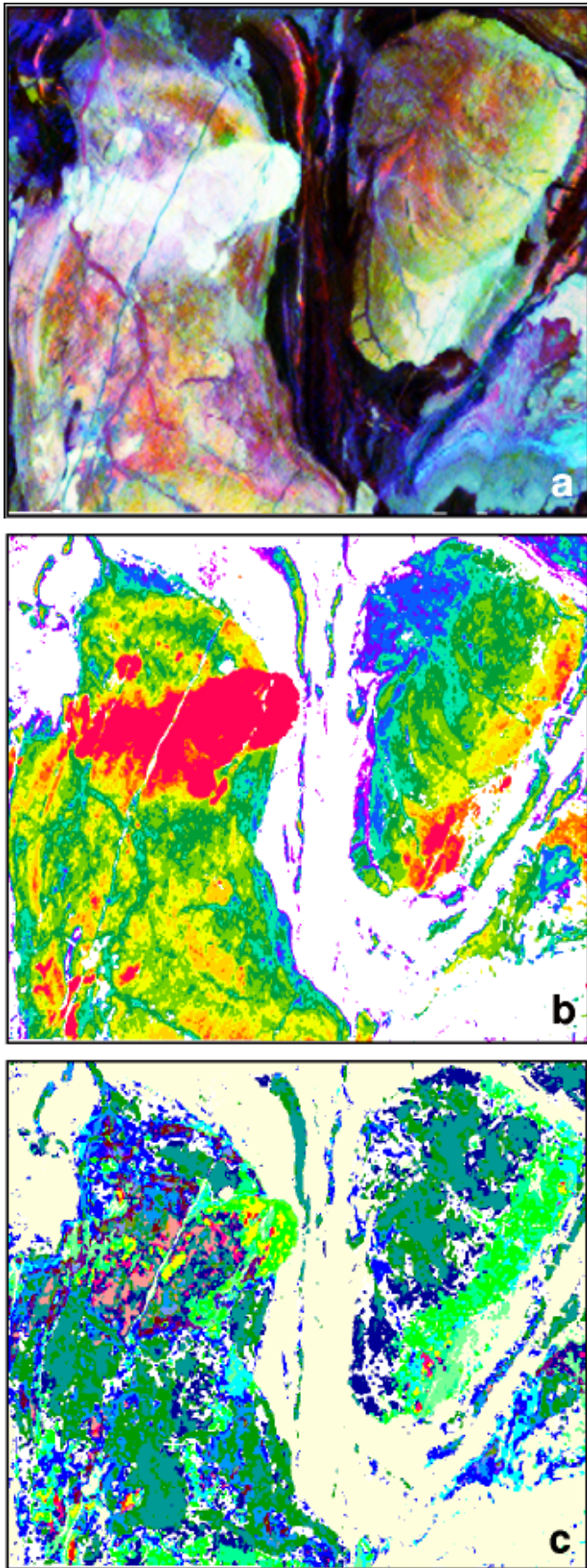
Click on each image for a larger version (Fig. 18. a–156k ; b–122k ; c–136k : Fig. 19. a–74k ; b–68k ; c–60k ; d–66k)

Fig. 18. Felsic igneous rocks of the Shaw and Corunna Downs Batholiths.
(a) **Traditional RGB display of K, Th, and U concentrations.** *(b)*
**Component showing the amount of differentiation: low differentiation
shown as blue, and high differentiation shown as red.** *(c)* **Components
showing differences of plus or minus more than one standard deviation
from the mean geochemical evolutionary path: K, Th, and U are red,
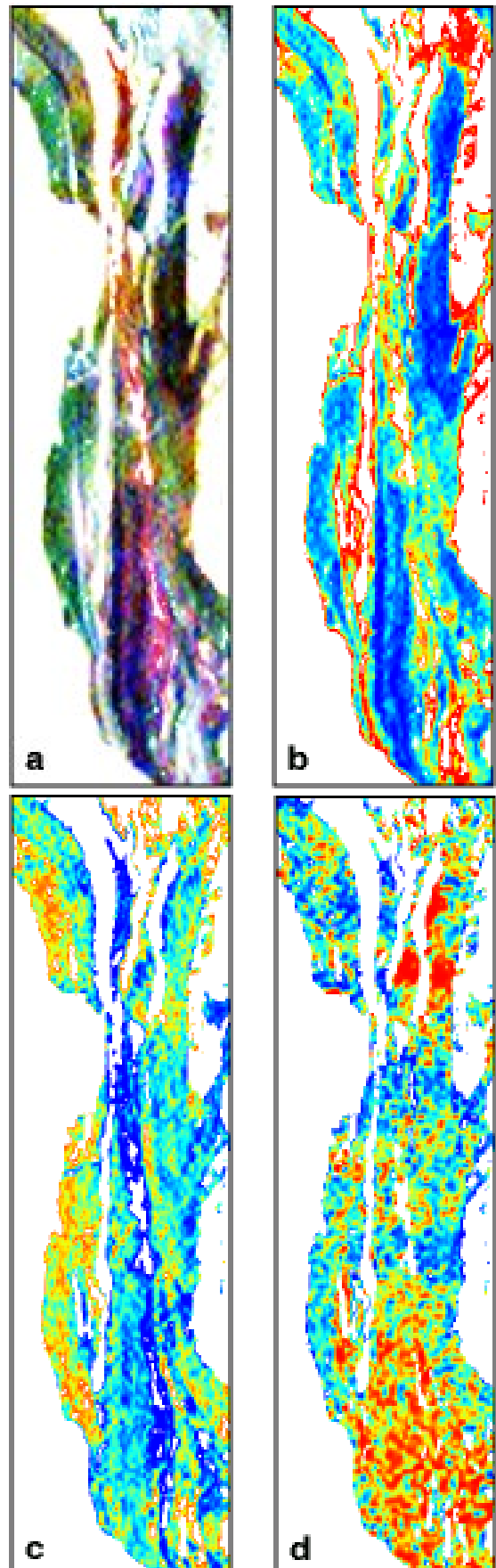green, and blue respectively. The area in the figure is 84 km wide.**

Fig. 19. Mafic igneous rocks of the Coongan Syncline. *(a)* **Traditional
RGB display of K, Th, and U concentrations. Fig. 19b–d shows separate
components as intensity — low values are blue; high, red.** *(b)* **Component
showing the amount of geochemical evolution.** *(c)* **Component showing
difference in Th content from the mean geochemical evolutionary path.**
(d) **Component showing difference in U content from the mean
geochemical evolutionary path. The area in the figure is 18 km wide.**

Using images in a geological interpretation of magnetic data

Songfa Liu[1] & Tim Mackey[1]

Many types of images can be produced from the magnetic data which are now routinely acquired for regional geological studies and mineral exploration. Different images enhance different features that enable the informed regional/exploration geologist to make full use of the data. Unfortunately, not all of the image types are readily available to the geologist, so vital geological information may remain untapped.

In this paper, we discuss the geological information that can be interpreted from magnetic data, and share our experiences of using images, in particular:

- the images used for the solid-geology interpretation of the Nabberu 1:250 000 Sheet area at the northeast margin of the Yilgarn Craton in Western Australia (Liu 1997: *AGSO Research Newsletter*, 27, 23–24), and
- anomaly-slope-enhanced images produced from a new method.

Lithostructural units

The geological interpretation of magnetic data involves identifying lithostructural units and structural features, all of which are best shown on a solid-geology map. For this purpose, images are the primary tool, although profile data are still needed for modelling. Magnetic lithostructural units define the lithological and structural features that can be interpreted from the magnetic data. Each lithostructural unit corresponds to a magnetic source or group of sources with characteristic magnetic patterns defined by the intensity and geometry of its magnetic sources. For many units, boundaries correspond to discontinuities in magnetic patterns, or sudden/sharp changes in intensity.

Owing to the different types and amounts of magnetic minerals they contain, different lithologies have different magnetic intensities, so they can be interpreted from a total magnetic intensity (TMI) image (Fig. 21a). Also, a considerable amount of structural information, particularly at macroscales, can be obtained from the distribution and geometry of magnetic sources. For a structural interpretation, it is important to determine the distribution and geometry of individual magnetic anomalies. Some apparently single, large anomalies are actually composites of several smaller ones. Special processing involving calculations of vertical derivatives may
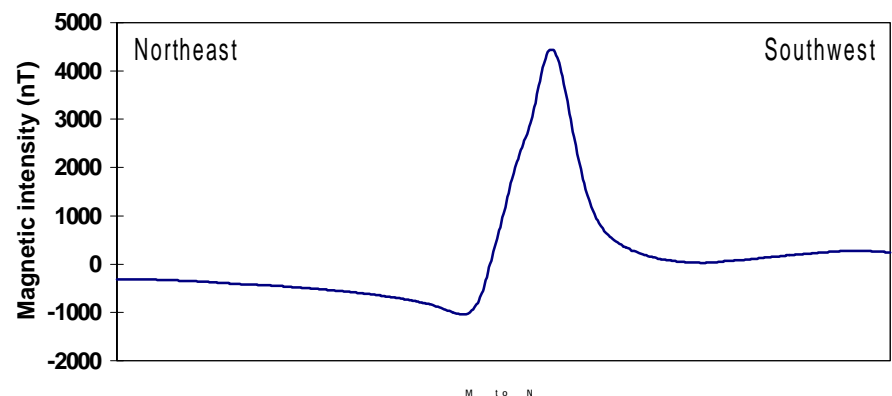

Fig. 20. Profile along line M–N crossing the highly magnetic BIF unit in Figure 21e. The asymmetry of the anomaly suggests that the unit dips to the northeast.

be needed to reveal individual anomalies. Vertical derivatives of TMI enhance high-frequency anomalies by 'sharpening' them. The first vertical derivative (Fig. 21b) appears to be most useful because it sharpens anomalies but does not enhance much of the noise in the data. For some composite anomalies, the second vertical derivative may have to be calculated to reveal further details, but this process also significantly enhances noise in the data. For some anomalies, an automatic-gain-control image may reveal additional structural information by amplifying and resolving weak signals (Rajagopalan & Milligan 1995: *Exploration Geophysics*, 25, 173–178). Many other image enhancement methods are available to assist resolving specific geological problems (Milligan & Gunn 1997: *AGSO Journal of Australian Geology & Geophysics*, 17, 63–75).

Our experience suggests that a TMI image (Fig. 21a) and a structurally enhanced (e.g., vertical derivative) image (Fig. 21b) are a useful combination for identifying different lithostructural units from the magnetic data.

Reduction to the pole

For individual magnetic anomalies, it is important to determine the location and geometry of their sources. For planar sources, their attitudes — vertical or dipping (and dip angle) — are important criteria. For this reason, magnetic data generally need to be reduced to the pole, particularly for areas close to the magnetic equator, in order to remove the asymmetry in magnetic anomalies due to the inclination of the Earth's magnetic field. Reduced-to-the-pole (RTP) data place anomalies directly above their sources.

This is consistent with the assumption that the magnetisation of the rocks in an area is by induction and no significant permanent magnetisation occurs in a direction other than that of the Earth's magnetic field. This assumption appears to hold for the Nabberu area because the images show no smearing 'comet tails', which occur where the assumption does not hold (MacLeod et al. 1993: *Exploration Geophysics*, 24, 679–688). Omitting this step can produce incorrect positions and geometries of geological features, particularly east-trending ones.

Colour and greyscale images

Colour images (Figs. 21a, d, and f) show anomaly magnitudes and long-wavelength features particularly well. However, small and low-magnitude anomalies may not be evident in colour images. The positions of colour changes are not only dependent on the positions, magnitudes, and widths of anomalies but also on how the data are assigned colours in image processing. Different colour lookup tables effect different colour distributions in an image. Furthermore, the human eye is easily distracted by the different colours (Fig. 21d). Consequently, the widths and boundaries of anomalies are hard to determine on colour images. A greyscale image (Fig. 21b) is more useful for showing fine details and locating anomaly boundaries. Even so, greyscale images do not give much indication of the magnitudes of anomalies.
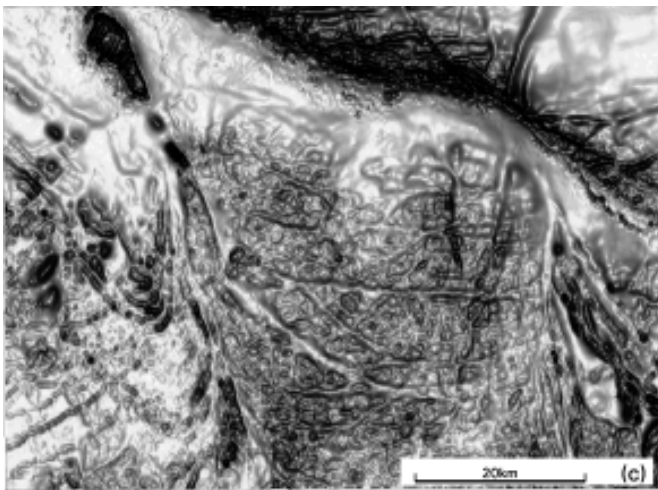
Anomaly slope images and contour maps

None of the images described above clearly defines the precise position of an
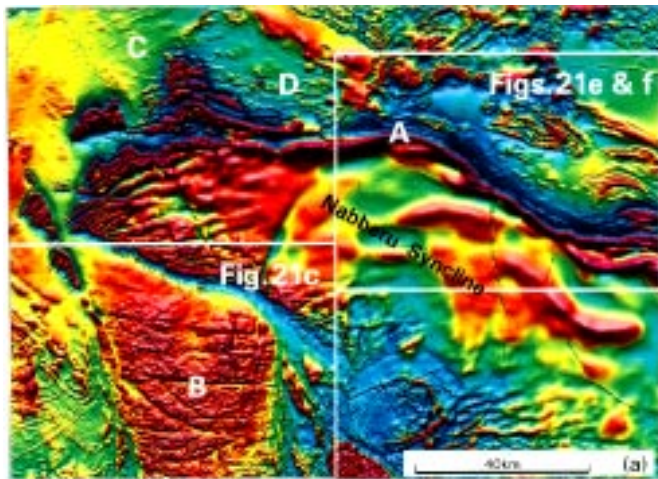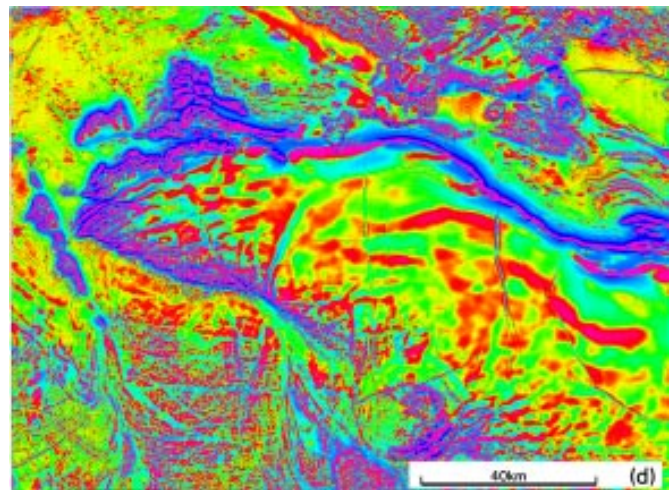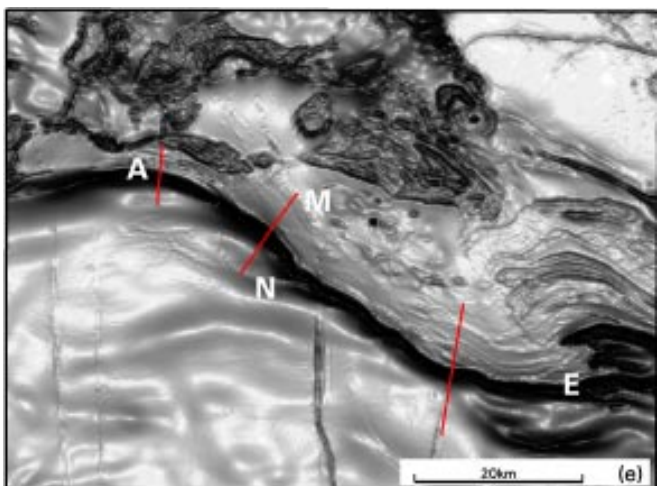
Click for larger image (162k)
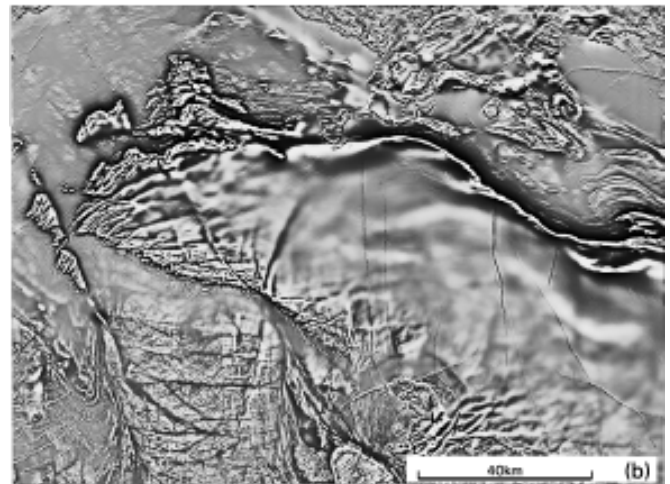
Click for larger image (108k)

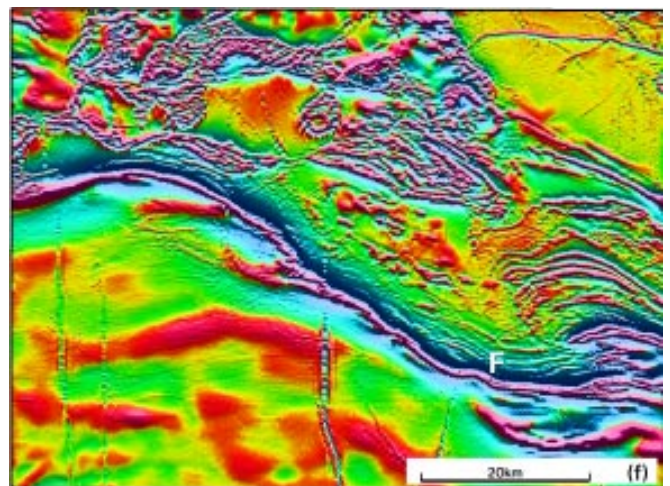*Click for larger image (89k)*

Click for larger image (228k)

Click for larger image (75k)

Click for larger image (208k)

Fig. 21. *(a)* **Total magnetic intensity image (TMI) of the Nabberu 1:250 000 Sheet area (data reduced to the pole for all images in this paper). This is a composite image based on the HSI (hue, saturation, intensity) colour model (Milligan et al. 1992:** *Exploration Geophysics***, 23, 219–224). It was derived from a colour image of TMI as hue and a greyscale image of TMI with northerly illumination as saturation and intensity. It combines the advantages of both colour and greyscale images with the highlight of features by illumination.** *(b)* **Greyscale image of the first vertical derivative of TMI for the Nabberu 1:250 000 Sheet area.** *(c)* **Greyscale anomaly-slope-enhanced TMI image of the Merrie area (compare with the southwest part of Fig. 21a). Anomaly peaks and valleys are bright (white), whereas slopes of anomalies show varying degrees of grey shades to black. The darker the shade, the steeper the anomaly.** *(d)* **Colour image of the first vertical derivative of TMI for the Nabberu 1:250 000 Sheet area.** *(e)* **Greyscale anomaly slope-enhanced TMI image of the Mount Cecil Rhodes area (northeast part of Fig. 21a). The BIF unit from positions 'A' to 'E' is much darker on the south side. This suggests that the unit dips north. Profile data from positions 'M' to 'N' are shown in Figure 20.** *(f)* **Colour composite image of the first vertical derivative of TMI with northerly illumination of the Mount Cecil Rhodes area (same area as Fig. 21e). Image produced by the same method as Figure 21a.**

anomaly's peak, which is important for correlating the anomaly with its geological source — particularly a linear one. Contour maps are traditionally used for this purpose. Although contour density helps determine the dip direction of an anomaly, contour maps have limitations because any chosen contour interval presents a compromise between showing high and low anomalies. In addition, unlike images, contour maps do not maintain data continuity.

We recently developed an anomaly-slope-enhancement method which produces images (Figs. 21c and e) that reflect the slopes and preserve the symmetry/asymmetry of an anomaly. In a greyscale image produced by this method, flat areas (e.g., peaks and valleys of anomalies) are shown as bright (white), while slopes are shown as various shades of grey to black; the darker the shade, the steeper the anomaly. The positions of both high and low anomalies can be precisely located. This method, therefore, facilitates close correlation of anomalies with their geological features. It also enables the dip direction of a planar source to be determined from the relative darkness and gradient on both sides of the anomaly. If a dyke-like planar source dips to the north, for example, the northern side of the anomaly will appear lighter than the southern side on the image. Because the symmetry/asymmetry of the anomalies is maintained in this type of image, it reflects a non-biased presentation of the enhanced structural features, unlike illuminated images, which highlight features at high angles to the illumination direction (Fig. 21c, compare with the southwest part of Fig. 21a). Therefore, this type of image assists a more objective structural interpretation.

Interpretation of the Nabberu area

Most lithostructural units in the Nabberu area are readily discernible from a colour TMI image for intensity (lithological) information (Fig. 21a) and a greyscale image of the first vertical derivative of TMI for structural information (Fig. 21b).

Anomaly-slope-enhanced images (Figs. 21c and e) are useful for structural interpretations and locating the positions of anomalies. Some illustrated examples follow.

The highly magnetic banded iron formation (BIF) of the Earaheedy Group ('A' in Fig. 21a; cf. 'A' to 'E' in Fig. 21e) defining the Nabberu Syncline has a moderate to steep dip on the northern limb, is gently dipping to subhorizontal on the southern limb, and youngs to the south. However, the anomaly is much darker on the southern side of the BIF from positions 'A' to 'E', suggesting that the bulk of the unit here dips north to northeast. This is confirmed by a profile across the anomaly (Fig. 20). Therefore, the bulk of the BIF here is overturned, dipping north but younging south; southerly dips, however, are apparent locally (Leech et al. 1977: Geological map, Nabberu 1:250 000 Sheet, Geological Survey of Western Australia).

A large granitoid body in the southwest of the Sheet area appears purple–red in the image ('B' in Fig. 21a). It abuts and underlies the hinge of the Nabberu Syncline, and continues to the northwest of the Sheet area but with lower magnetic intensity (shown in yellow and greenish blue — e.g., at position 'C').

The magnetic pattern in the area around 'D' (Fig. 21a) shows features that can be attributed to both the highly magnetic BIF unit and the underlying granitoid. The low magnetisation of the area as shown in the TMI image (Fig. 21a) is attributed to the underlying granitoid. However, the linear east-trending anomalies in this area are similar to that of the BIF west and south of this area (Figs. 21a and b). These features led Liu (1997) to interpret the magnetic BIF in area 'D' as thin.

Further detailed interpretation can be done with more specifically processed images. Pseudo-illumination can highlight some features, particularly low-magnitude anomalies that may not be evident in images without illumination. Thus, in area 'F', north of the highly magnetic BIF (Fig. 21f), several small, low-magnetic anomalies trend subparallel

to this unit. They are clearly shown in the northerly illuminated image of the first derivative of TMI (Fig. 21f), but are less evident in images without illumination (Fig. 21b). Recognising such differences, the interpreter should be aware of a potential bias due to the illumination, which highlights features at high angles to the direction of its source. For example, in the Merrie area, structures are oriented in all directions, as shown in the anomaly-slope-enhanced image (Fig. 21c), which shows a non-biased presentation of structures. In the northerly illuminated TMI image of Figure 21a, however, east–west trending features are enhanced at the expense of anomalies in other directions. Therefore, for illuminated images, several illumination directions/angles may be needed to highlight features trending in different directions. Even so, a geological interpretation of magnetic data should not rely solely on illuminated images, which should be used in conjunction with other images in order to present a balanced representation of key geological features.

Concluding remarks

Although many types of images can be produced from magnetic data, two or three types provide most of the geological information that can be obtained from the data. They include a colour TMI (RTP) image, a greyscale vertical derivative of TMI (RTP) image, and a greyscale anomaly-slope-enhanced image of TMI (RTP). As interpretation becomes more specific, other types of images may be produced for interpreting geological detail.

Acknowledgments

[1] Minerals Division, Australian Geological Survey Organisation, GPO Box 378, Canberra, ACT 2601; tel. +61 2 6249 9522 (SL), +61 2 6249 9813 (TM); fax +61 2 6249 9971 (SL), +61 2 6249 9913 (TM); e-mail sliu@agso.gov.au, tmackey@agso.gov.au.

Average composition of the crust in the Australian, Fennoscandian, and Ukrainian shields from refraction seismic studies and petrophysical modelling

Alexey Goncharov[1], Barry Drummond[1], Alexander Tripolsky[2], & Lesley Wyborn[3]

Seismic velocity models of the Australian, Fennoscandian, and Ukrainian shields[*] fall into two broad categories: one has thin (35–44 km) crust; the other, thick (>45 km). In the Australian shield, Archaean crust is identified as thin; Proterozoic crust, as thick. The Ukrainian shield is the only one whose average models of both thick and thin crust show remarkably similar velocities in the upper 44 km of the crust. Velocities in the upper 20 km of the Ukrainian shield are noticeably higher than in other regions. The hottest assumed geotherm among the regions analysed is that of the Australian Proterozoic crust. Differences in seismic velocity distribution in the crust of the three Precambrian domains do not necessarily translate into marked differences in composition if the differences in geothermal regimes are considered.

The crust of the Fennoscandian and Ukrainian shields has been studied from a network of seismic profiles which is more dense than networks in many other parts of the world. This facilitated the development of detailed seismic models of the crust of these regions (Tripolsky 1996: Geophysical Journal (National Academy of Sciences, Ukraine), 16, 23–47; Goncharov et al. 1998: AGU Geodynamics Series, 26, 119–138). Significant parts of the north Australian Precambrian craton and Archaean Yilgarn Block in Western Australia have been studied by refraction and wide-angle reflection seismic profiles, although the density of observations is less than in the other shields. Seismic velocity models of the Australian Precambrian were summarised by Collins (1988: BMR/ AGSO Report 277) and interpreted by Drummond & Collins (1986: Earth and Planetary Science Letters, 79, 361–372). We limited this study to the region above the Moho[†].
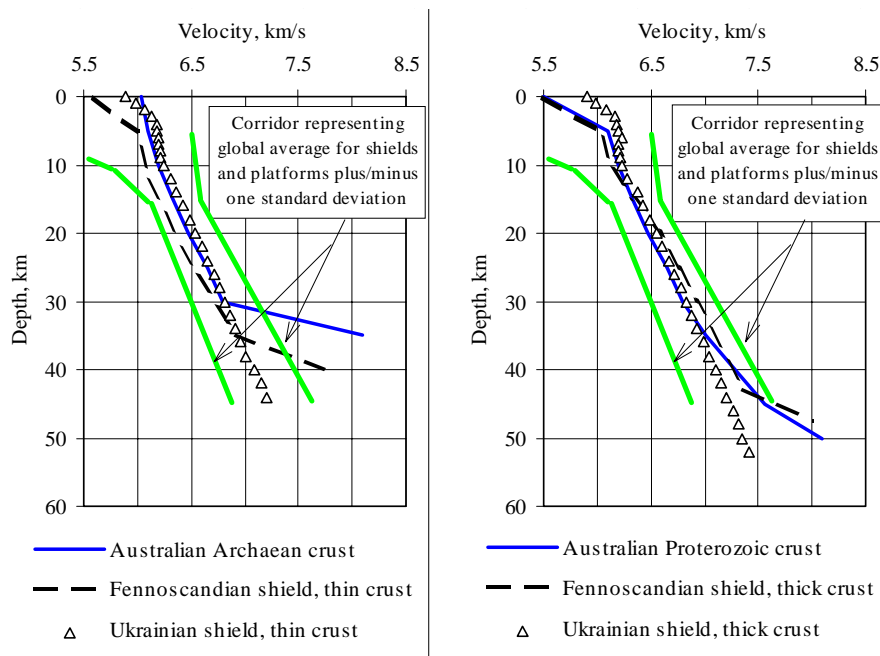

Fig. 22. Average velocity models of the Australian, Fennoscandian, and Ukrainian shields compared with the global average model for shields and platforms (Christensen & Mooney 1995: op. cit.).

Velocity models

Velocity models of all three regions fall into two broad categories: one has thin crust (35–44 km); the other, thick (>45 km; Fig. 22). Crustal velocities in the Fennoscandian thin crust are slightly lower, and in the thick crust slightly higher, than in the global average model for shields and platforms (Christensen & Mooney 1995: Journal of Geophysical Research, 100, B7, 9761–9788). The total thickness of the crust in the Fennoscandian shield is close to the global average value (41.5 km) in the thin crust model, but noticeably higher in the thick crust model, in which the shallowest Moho was defined at 45 km depth. The Australian Archaean crust is on average thinner (about 35 km) than in the global average model, and generally thinner than the Australian Proterozoic crust.

In the Australian shield, the increase in total crustal thickness correlates with

an increase in seismic velocity starting at 30 km depth in the lower crust. In the Fennoscandian shield, velocities from 10 km down to the Moho are higher in the thick crust model than in the thin model. Of the three shields, the Ukrainian shield is the only one in which average velocity models of both thick and thin crust are remarkably similar through the whole crust, and the velocity–depth function of the thick crust below 44 km depth is a continuation of the trend typical for the thin crust. Velocities in the Ukrainian shield are noticeably higher in the upper 20 km but lower in the lower part of the crust compared with the other regions analysed (Fig. 22).

Low-velocity layers are quite common in the crust of the Fennoscandian shield. They were also recognised in some interpretations from the Australian shield (Finlayson 1982: Journal of Geophysical Research, 87, 10569–10578; Goncharov et al. 1997: AGSO Research Newsletter, 26, 13–16.). In the Ukrainian shield, they are mainly restricted to the upper crust (Tripolsky 1996: op. cit.). Low-velocity layers were ignored in the smoothed velocity models used for the petrological interpretation below (Fig. 22).

---

[*] Results from the Australian and Fennoscandian Shields were discussed at the workshop on Palaeoproterozoic tectonics and metallogenesis held in Darwin in September 1997 (Rutland & Drummond, Editors, 1997: AGSO Record 1997/ 44).

[†] Griffin & O'Reilly (1987: Geology, 15, 241–244) make a distinction between the Moho, whose formal definition is a seismic discontinuity, and the petrologically defined boundary between the crust and mantle. In this paper, we follow the formal definition of the Moho.
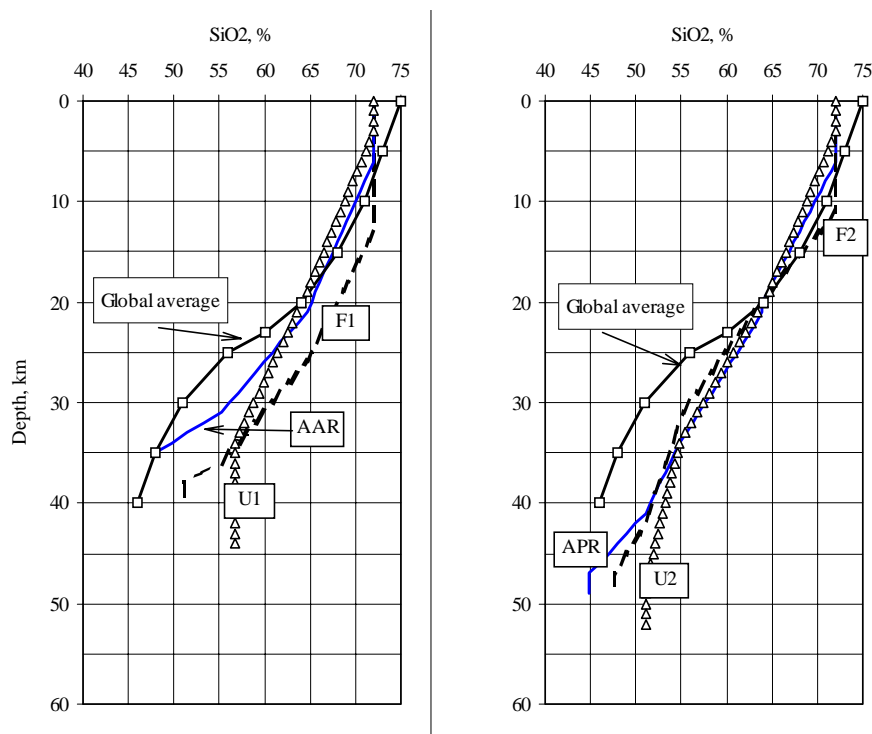
Fig. 23. SiO₂ distribution in the crust of the Australian, Fennoscandian, and Ukrainian shields compared with the global average model (Christensen & Mooney 1995: op. cit.). The abbreviations of the model names are the same as those in Table 2.

Methodology for the petrological interpretation of velocity models

The six velocity models (Fig. 22) are representative of the three shields under consideration. They were interpreted in terms of the bulk geochemistry of rocks at depth. The petrophysical modelling technique of Sobolev & Babeyko (1994: Surveys in Geophysics, 15, 515–544) was used to predict seismic velocities at depth for a range of assumed crustal compositions; it was used earlier to interpret the composition of the crust in the Mount Isa Inlier (Goncharov et al. 1997: op. cit.). The method considers igneous rocks only, and the possibility of metasediments in the deep crust is ignored.

An important feature of our approach was that we treated the crust as a mixture of a limited number of rock types ('granites', 'diorites', 'gabbros', and 'spinel lherzolites') represented by their end-members. The bulk geochemical composition within each rock type was kept constant, and the mineralogical compositions allowed to vary, to account for equilibration at the likely prevailing pressures and temperatures during rock formation. Thus, the technique accounts for the changing mineral assemblages from plagioclase-bearing and garnet-free to garnet-bearing and plagioclase-free.

Our petrological interpretation gave us an estimate of the proportion of the various rock types at a number of depth ranges that have the appropriate seismic velocities (ranging in steps of 0.4 km/s from 5.7 km/s near the surface to 8.1 km/s at the Moho) observed in the models.

Temperature regimes of the crust

This approach required an estimate of the likely pressure and temperature conditions in the modern crust. The pressure–depth function that we used was computed for an assumed mean crustal density of 2.830 t/m³, a global average for continental crust (Christensen & Mooney 1995: op. cit.). The thermal regime of the crust affects seismic velocity at depth more significantly than pressure. The Australian Proterozoic crust has an estimated thermal regime hotter than the others (Fig. 24) because its surface heat flow of 60 mW/m² (Cull 1991: Geological Society of Australia, Special Publication, 17, 147–155) is well above the average value of 40 mW/m² in the other regions.

Accuracy of the petrological interpretation of seismic velocities

Uncertainties in the estimates of crustal composition arise from uncertainties in the measured seismic velocities and uncertainties in the estimated palaeo- and modern temperatures in the crust. At high pressures and temperatures, the amount of plagioclase in the equilibrium mineralogy of a cooling magma increases with increasing equilibrium temperature at a fixed pressure. Hence, the higher the

Table 2. Composition of the Australian Archaean (AAR), Australian Proterozoic (APR), Fennoscandian thin (F1), Fennoscandian thick (F2), Ukrainian thin (U1), and Ukrainian thick (U2) crust interpreted from average seismic models

Depth (km)	Model type	Rock type (%)*				Notes
		'Granite'	'Diorite'	'Gabbro'	'Spinel lherzolite'	
0–10	All models	100±0†	0	0	0	
10–20	AAR, F2	85±15	15±15	0	0	
	APR	100±0†	0	0	0	
	F1	95±5	5±5	0	0	
	U1, U2	80±20	20±20	0	0	
20–30	AAR	45±15	55±5	10±10	0	
	APR	40±40	60±40	0	0	
	F1	70±25	30±25	0	0	
	F2	45±30	55±5	15±15	0	
	U1, U2	45±25	55±5	15±15	0	
30–40	AAR	0	25±15	70±20	20±20	Down to 35 km only
	APR	15±15	55±5	35±20	0	
	F1	20±20	40±5	40±25	5±5	
	F2	0	55±30	45±30	0	
	U1	15±15	70±20	25±25	0	
	U2	15±15	50±5	35±15	0	
40–50	AAR	N/A	N/A	N/A	N/A	
	APR	0	10±10	65±5	35±25	
	F1	N/A	N/A	N/A	N/A	
	F2	0	5±5	75±20	20±20	Down to 49 km only
	U1	0	50±50	50±50	0	Down to 44 km only
	U2	0	35±35	65±35	0	Down to 52 km

* Rounded to the nearest multiple of 5% value.
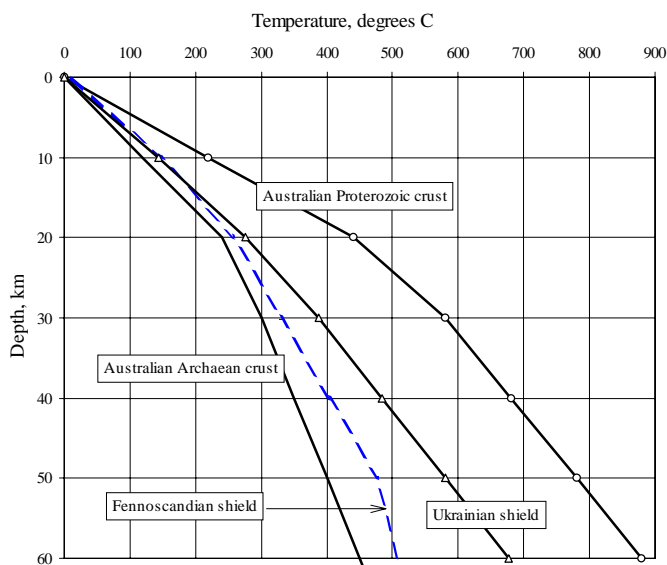† Based on an assumption (see the text).

Fig. 24. Temperature in the crust of the Australian Archaean and Proterozoic domains of Cull (1991: op. cit.), and the Fennoscandian (Glaznev et al. 1997: Geophysical Journal (National Academy of Sciences, Ukraine), 19 (4), 57–60) and Ukrainian shields (Kutas 1993: Lithosphere of central and eastern Europe (in Russian), Naukova Dumka, 114-135).
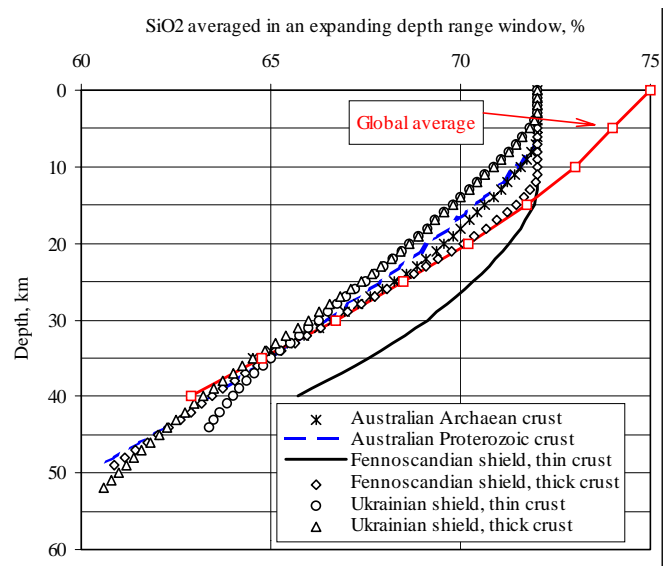

Fig. 25. SiO₂ distribution in the crust of the Australian, Fennoscandian, and Ukrainian shields averaged in an expanding depth-range window compared with the global average model (Christensen & Mooney 1995: op. cit.). The top of the expanding window was kept at the surface, and the bottom of the window gradually shifted downwards; averaged values are plotted against the depth of the bottom of this window, and hence represent average SiO₂ content from 0 km to any given depth.

equilibrium temperature during rock formation, the lower the velocity of the rock. This is the reason why the velocities vary within each group of rocks analysed — for example, 'gabbros' may have velocities ranging from 7.25 to 7.70 km/s at 30 km depth under the modern temperature regime of the Australian Archaean crust; this velocity range reflects the uncertainty in the palaeotemperature estimate of about 200°C at that depth, and is representative of the uncertainties typical for the other rock types. We did not systematically test the uncertainty which the variation in palaeotemperatures imposes on our petrological interpretation, because our probabilistic approach to the estimation of bulk crustal composition accounts for this uncertainty.

Modern crustal temperatures which affect the interpreted bulk composition are estimated from surface heat flow, based on assumptions about the distribution of heat-producing elements at depth. An increase in surface heat flow of 10 mW/m² translates into an increase of ~100°C in the temperature estimate at mid-crustal level. This in turn results in a 0.05 km/s decrease in seismic velocity value predicted by petrophysical modelling for a constant mineralogy. This is about one-fifth of one standard deviation of the average velocity models shown in Figure 22.

To estimate the combined effect of both velocity and modern temperature

uncertainties on the accuracy of the petrological interpretation, we modelled the most unfavourable situation — that in which underestimated experimental seismic velocities are compared with the overestimated velocities predicted by the petrophysical modelling, and vice versa. The petrophysical modelling overestimates velocities when temperatures in the crust are underestimated. So the biggest error in the petrological interpretation will happen when seismic velocities and temperatures are both lower or both higher than the original distributions of Figures 22 and 24. We used a variation of 0.2 km/s in velocities and a temperature variation of up to 200°C in the lower crust. These differences reflect the range of velocities in Figure 22 and the uncertainties in estimated modern temperatures (Fig. 24). The resulting uncertainties in the petrological interpretation are shown in Table 2.

Petrological models of the crust

Table 2 presents the likely composition of the layers in the resulting petrological models. Seismic velocities in some layers in the upper crust are too low to be explained by the intrinsic properties of pure anhydrous rocks of granitic composition. Such low velocities may be due to open cracks and pores (assumed for further computations), or to

metasediments (not modelled by this technique), whose hydrous phases and greater pore volume would result in velocities lower than in granitic rocks.

The bulk geochemistry of the rocks in all six models varies from 100% 'granite' composition in the upper 10–20 km of the crust to a mixture of mafic and ultramafic rocks in the lower 10 km. The SiO₂ content for each layer was also estimated. The top part of the crust in all our models contains about 72% SiO₂ — i.e., it is more felsic than suggested in some other studies based on the petrology and geochemistry of rock samples: 66-67% (Condie 1993: Chemical Geology, 104, 1–37), 66% (Taylor & McLennan 1985: The continental crust: its composition and evolution, Blackwell, London), and 65% (Shaw et al. 1986: Geological Society of London, Special Publication 24, 275–282). An obvious explanation for these discrepancies would be the limitations of our approach. Nevertheless, the upper crust in the global average model of Christensen & Mooney (1995: op. cit.) is even more felsic than in our models (Fig. 23), although their approach did account for the possible presence of metasedimentary rocks in the crust, and it did take seismic data into consideration as well. Therefore we conclude that further research is needed to investigate how other rock types can be incorporated into our methodology without disrupting its integrity.

Velocities in the Australian

Proterozoic, Fennoscandian thick, and Ukrainian thick crust require a >15-km-thick layer of rocks containing less than 55% SiO_2 (Fig. 23) in the lowermost crust. This content corresponds to a dioritic to gabbroic bulk composition of the lower crust. In contrast, the Fennoscandian thin crust and Australian Archaean crust require no more than 5 km of such rock in the lowermost crust. The lower part of the Ukrainian thin crust requires no such rock at all.

More significant variations in SiO_2 content are observed within the group of thin crustal models — e.g., in the upper part of the Fennoscandian thin crust model, SiO_2 is systematically higher than in the other models. Models of thick crust are more uniform in SiO_2 distribution, although the lower part of the Ukrainian thick crust is up to 5% more felsic than in other models in this category (Fig. 23). Owing to the low temperatures in the Ukrainian shield, the relatively high velocities in the upper part of the crust there (Fig. 22) do not translate into a composition noticeably more mafic than the Australian Proterozoic crust (Fig. 23). The average whole-of-crust SiO_2 content

in all models of thin crust is 63.3–65.7%, which is higher than in the global average model (61.8 %) of Christensen & Mooney (1995: op. cit.). Our thick crustal models have SiO_2 content close to the global average value (Fig. 25).

Analysis of SiO_2 content averaged in an expanding depth-range window (Fig. 25) clearly shows that the curves for all models except that for the Fennoscandian thin crust merge to within 0.5 per cent at a depth of 35 km (at a depth level of the shallowest Moho in the Australian Archaean average model). This means that, although differences in composition occur throughout the crust, the averaged SiO_2 content in the upper 35 km of the Precambrian crust analysed is the same for all models, except the Fennoscandian thin crust. At province scale, we have also observed that the averaged SiO_2 content in the upper 45 km of the crust (about 10 km above the Moho) in the Mount Isa Inlier is remarkably constant (Goncharov et al. 1997: op. cit.).

The key conclusion of this work is that Precambrian crust, particularly in the top part, has a remarkably constant overall

composition, and that the apparent differences in seismic models between the shields can mostly be explained by different thermal regimes affecting equilibrium mineralogies at depth. Geological explanations of why this should be so require further studies.

Acknowledgment

[1] Petroleum & Marine Division, Australian Geological Survey Organisation, GPO Box 378, Canberra, ACT 2601; tel. +61 2 6249 9595 (AG), +61 2 6249 9381 (BD); fax +61 2 6249 9972; e-mail agonchar@agso.gov.au, drummond@agso.gov.au.

[2] Division of Regional Geophysics, Institute of Geophysics National Academy of Sciences, Palladina 32, Kiev, 252680, Ukraine; fax +380 44 450 2520; e-mail root@igpnanu.kiev.ua.

[3] Minerals Division, Australian Geological Survey Organisation, GPO Box 378, Canberra, ACT 2601; tel. +61 2 6249 9489; fax +61 2 6249 9971; e-mail lwyborn@agso.gov.au.

Shrimp U–Pb dating of ignimbrites in the Pul Pul Rhyolite, Northern Territory

A cautionary tale

Elizabeth Jagodzinski[1]

Isotopic dating of volcanic rocks in sedimentary sequences has a wide variety of applications, as the data can provide direct numerical ages to complement stratigraphic, basin analysis, and timescale studies. The primary eruptive products of silicic volcanic centres are pyroclastic fall deposits (tuffs), pyroclastic flow deposits (ignimbrites), and small-volume rhyolite lavas. Ignimbrites are the most voluminous of these volcanic products. They are laterally extensive, have good preservation potential, and generally form the dominant component of ancient volcanic successions. For these reasons, they are likely to be a common target for the dating of volcanic complexes and stratigraphic sequences. However, of all the primary volcanic facies, ignimbrites present the most difficult dating prospect because they are the products of violent and explosive volcanic activity, and the pyroclastic flow commonly assimilates large volumes of country rock during eruption and deposition. It is important to be aware that geochemical and geochronological analyses of ignimbrites are therefore subject to considerable error because these xenoliths can introduce inheritance into the zircon population. Inheritance presents a widely recognised problem in U–Pb age-dating studies, as the crystallisation ages of complex zircon populations with polymodal age distributions can be difficult to resolve.

Sample constraints for dating the Pul Pul Rhyolite

A geochronological study of the Pul Pul Rhyolite (Pine Creek Inlier, NT) highlights some of the problems that can be encountered in obtaining a stratigraphic age for a lithic-rich ignimbrite sequence. The Pul Pul Rhyolite is a volcanic formation of the El Sherana Group, which comprises a thick (830 m) sequence of ignimbrites and minor volcaniclastic rocks and intrusive rhyolite porphyries. The ignimbrites contain a high proportion of lithic contamination —including basalt,

Click for a larger image (21k)

Fig. 26. A summary of the data obtained for all samples analysed in this study. The left-hand column compares histograms of the ^{207}Pb/^{206}Pb ages obtained for each sample, and illustrates how lithic contamination increases the complexity of the zircon populations (only ages less than 2000 Ma are plotted).

porphyry, sandstone, granite, chert, and metasedimentary basement clasts, most of which are potential sources of zircon contamination.
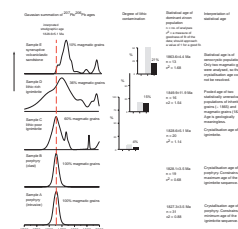
Three samples from the volcanic sequence containing varying degrees of lithic contamination were selected for U–Pb dating: lithic-poor (4% lithic constituents; sample C in Fig. 26) and lithic-rich ignimbrites (15% lithic constituents; sample D) and a syneruptive volcaniclastic rock (21% lithic constituents; sample E) were selected to determine the effect of xenolithic contamination on the zircon populations. In addition, two samples of quartz–feldspar porphyry were selected to provide independent control on the age of the ignimbrite sequence: an intrusive porphyry to constrain the minimum age of the ignimbrites (sample A), and a large porphyry clast extracted from an

ignimbrite breccia to provide a maximum constraint (sample B). In contrast to the ignimbrites, the porphyries were expected to contain simple zircon populations because they contain no visible lithic contamination.

Results

As expected, the two coherent quartz–feldspar porphyry samples (A and B) are free of lithic contamination and contain zircons of uniform age (Fig. 26), indicating their zircon populations contain only magmatic grains and no older xenocrysts. In contrast, the zircon populations of the lithic-contaminated samples have complicated isotopic patterns that reflect inherited components of more than one age.

The ages of the two porphyry samples are identical within analytical uncertainty. They tightly constrain the eruption of the

Gaussian summation of $^{207}Pb/^{206}Pb$ ages

Degree of lithic contamination

Statistical age of dominant zircon population
n = no. of analyses
c^2 = a measure of goodness of fit of the data; should approach a value of 1 for a good fit.

Interpretation of statistical age

interpreted stratigraphic age
1828.6±5.1 Ma

Sample E
syneruptive volcaniclastic sandstone

10% magmatic grains

21%

1863.6±4.4 Ma
n = 13
c^2 = 1.68

Statistical age is of xenocrystic population. Only two magmatic grains were analysed, so the crystallisation age could not be resolved.

Sample D
lithic-rich ignimbrite

36% magmatic grains

15%

1849.9±11.9 Ma
n = 16
c^2 = 1.54

Pooled age of two statistically unresolvable populations of inherited grains (~ 1865) and magmatic grains (1826 Ma). Age is geologically meaningless.

Sample C
lithic-poor ignimbrite

60% magmatic grains

4%

1828.6±5.1 Ma
n = 20
c^2 = 1.14

Crystallisation age of ignimbrite.

Sample B
porphyry (clast)

100% magmatic grains

1828.1±3.5 Ma
n = 19
c^2 = 0.68

Crystallisation age of porphyry. Constrains the maximum age of the ignimbrite sequence.

Sample A
porphyry (intrusive)

100% magmatic grains

1827.3±3.5 Ma
n = 31
c^2 = 0.89

Crystallisation age of porphyry. Constrains the minimum age of the ignimbrite sequence.

1700 1750 1800 1850 1900 1950 2000

Age (Ma)

ignimbrite sequence between 1828.1 ± 3.5 and 1827.3 ± 3.5 Ma. Only one ignimbrite sample containing the least amount of xenolithic contamination (sample C) yielded a well-defined magmatic age of 1828 Ma (sample C). In this lithic-poor ignimbrite, 60 per cent of the 33 grains selected for analysis are of magmatic origin, and the combined analyses of these grains indicate that the melt-precipitated zircons crystallised at 1828.6 ± 5.1 Ma. In contrast the inheritance is so pronounced in the zircon populations of the two samples with the highest degree of lithic contamination that their magmatic ages could not be determined. It is important to note that inherited grains dominate the zircon populations of these lithic-rich samples, even though the analytical strategy was to target melt-precipitated grains. This is because the inheritance is dominated by the youngest xenocrystic population, which could not be detected optically because the zircons comprise euhedral, prismatic, oscillatory-zoned magmatic grains with a similar form to the melt-precipitated 1828-Ma grains.

It is the presence of this youngest xenocrystic population that complicates the interpretation of the data in the most contaminated samples. The significantly older inherited grains do not present a problem as they can be clearly identified as xenocrysts and not part of the melt-precipitated zircon population. The youngest xenocrystic population however, has a weighted mean age of 1865 ± 3 Ma, which is only ~40 m.y. older than the melt-precipitated zircon population (this age is based on the combined analyses of grains belonging to this population from all samples; n = 23, χ^2 = 1.34).

In sample C (lithic-poor ignimbrite), the 1865-Ma xenocrysts did not present a problem when determining the crystallisation age of the sample. Only three 1865-Ma xenocrysts were analysed, and were rejected as statistical outliers to the main crystallisation population, which comprised 20 grains.

In sample D (lithic-rich ignimbrite) however, roughly equal proportions of melt-precipitated grains and grains belonging to the 1865-Ma xenocryst population were analysed (9 and 7 grains respectively). The combined 16 analyses of the two age groups yielded a weighted mean age of 1849.9 ± 11.9 Ma. The χ^2 value of 1.54 for the 16 analyses indicates they conform to a single statistical population. Despite this fact, the gaussian histogram for this sample shows excess scatter for a single peak. The data are clearly skewed towards lower $^{207}Pb/^{206}Pb$ ages, and do not approach a normal distribution as a single statistical population should. If this sample were analysed in isolation, this bias towards lower ages would probably have been attributed to Pb-loss, and the statistical age of 1849.9 ± 11.9 Ma would have been accepted as the crystallisation age of the ignimbrites.

In the context of the other samples, this age is too old, and the data are interpreted in an entirely different manner. The single statistical population is interpreted to comprise two age groupings which can be seen on the gaussian histogram, but cannot be statistically resolved. The statistical population can be deconvolved into two components which have ages of 1861.9 ± 15.7 Ma (based on the 7 oldest grains) and 1810.3 ± 26.8 Ma (based on the 9 youngest grains). These two age groupings are interpreted to represent the 1865-Ma xenocrystic population, also apparent in samples C and E, and the magmatic zircon population respectively. The interpreted magmatic population is younger than the crystallisation age of the sequence as defined by the porphyries and ignimbrite sample C (1828 Ma), but is based on only nine analyses, and the large error indicates the age is poorly defined. If the nine analyses are combined with data from the other ignimbrite sample (C), they statistically conform to the normal population at 1828 Ma.

In the syneruptive volcaniclastic sandstone (sample E), which contains the most lithic contamination of all samples analysed, the inherited population has an even more significant influence on the analytical results, as the dominant zircon population comprises 1865-Ma xenocrysts. Only two of the grains analysed were identified as possibly belonging to the magmatic zircon population. These two grains were identified as statistical outliers to the main zircon population at 1863.6 ± 4.4 Ma (based on 13 xenocrystic grains). If this sample had been analysed in isolation, the main zircon population would not have been recognised as xenocrystic, and the age of the Pul Pul Rhyolite would have been taken to be 1863.6 ± 4.4 Ma, which is ~40 m.y. too old.

Conclusions and implications

The U–Pb analysis of the different facies of the Pul Pul Rhyolite has shown that:

- the ignimbrites and intrusive quartz–feldspar porphyries are essentially comagmatic, and crystallised at 1828 Ma, and
- the country rock incorporated into the ignimbrites and volcaniclastic rock contained sources of more than one age, including one ~40 m.y. older than the Pul Pul Rhyolite sequence.

The age of this inherited population is interpreted to be ~1865 ± 3 Ma. The stratigraphic age of the Pul Pul Rhyolite is taken from the magmatic population of the lithic-poor ignimbrite, which is 1828.6 ± 5.1 Ma.

The results of this study have two important implications for the dating of ignimbrites and other facies which contain significant crustal contamination:

- Firstly, it is important to minimise the degree of lithic contamination in samples selected for geochronological analysis. The study has shown that the crystallisation age of the samples can become more difficult to interpret as the degree of lithic contamination increases.
- Secondly, when interpreting the age of samples containing multiple age populations, the geochronological data cannot be considered in isolation from other data sets and available geological constraints. Without the independent geological constraints on the age of the volcanic sequence supplied by the porphyry samples, the age of the most lithic-rich clastic samples would have been misinterpreted.

[1] Minerals Division, Australian Geological Survey Organisation, GPO Box 378, Canberra, ACT 2601; tel. +61 2 6249 9613; fax +61 2 6249 9983; e-mail ejagodzi@agso.gov.au.

New Nd-isotopic and geochemical data from the west Pilbara

Implications for Archaean crustal accretion and shear zone movement

Shen-su Sun[1] & Arthur H. Hickman[2]

Neodymium-isotope model ages of felsic igneous rocks offer information about the crustal residence times of their source rocks. Integrated with igneous emplacement ages from SHRIMP zircon U–Pb dating, this information reveals that juvenile crust formed at different times in the east and west Pilbara Craton. Geochemical characteristics of felsic and mafic igneous rocks from the west Pilbara, combined with the new isotopic data, offer some constraints for resolving outstanding issues: (1) Did plate teconics and terrane accretion play major roles in the formation of the Pilbara Craton?; and (2) How important is the Sholl Shear Zone as a geological boundary in the west Pilbara?

The 'North Pilbara' NGMA project* has been combining regional geological mapping and SHRIMP zircon U–Pb dating (Nelson 1996, 1997: Geological Survey of Western Australia, GSWA, Records 1996/5 and 1997/2) with research carried out at the University of Western Australia. As a result, it has demonstrated that most (if not all) rock sequences in the west Pilbara have no stratigraphic equivalents in the east Pilbara; clarification of this observation awaits geochronological and geochemical data for specific east Pilbara volcanic contemporaries (e.g., from the Strelley and Gorge Creek Groups) of the west Pilbara (Roebourne Group).

In the west Pilbara, Hickman (1997: GSWA, Annual Report, 76-81) has revised the greenstone stratigraphy of the Roebourne–Whundo area (Fig. 27). The oldest dated rocks, 3270 to 3250 Ma, are restricted to the area north of the Sholl Shear Zone (SSZ), a major structural feature between Port Hedland and Karratha. Between 3270 and 3260 Ma, the Karratha Granodiorite (Smith et al. in press: Precambrian Research; Nelson in press: GSWA, Records) intruded an older supracrustal sequence (Ruth Well Formation, part of the Roebourne Group) containing aluminium-depleted komatiites. Smith et al. (in press: op. cit.) suggest that this igneous complex was formed in an island-arc setting. The Ruth Well Formation must exceed 3270 Ma, but as it is conformable with the overlying ca 3270 Ma Nickol River Formation (Hickman 1997: op. cit.) it is probably not much older.

These rocks are ~200 Ma younger than the oldest dated rocks in the east Pilbara, represented by the widespread Warrawoona Group (3430–3470; e.g., Krapez 1993: Precambrian Research, 60, 1–45).

In the Roebourne area, the SSZ separates the Roebourne Group from the younger Whundo Group (Fig. 27). There is no consensus about the total distance of its movement and tectonic significance. GSWA work indicates a major early (pre-3020 Ma) sinistral movement followed by (post-2925 Ma) dextral movement of 30 to 40 km (Hickman in preparation: Explanatory notes for the Dampier 1:250 000 geological map, GSWA). According to SHRIMP zircon U–Pb dating of granites in the SSZ and rocks on both sides of it, Smith et al. (in press: op. cit.) suggest that two domains were juxtaposed at about 2960 Ma by the largely sinistral SSZ. This interpretation implies that the SSZ is a terrane boundary dating from that time, but GSWA geochronological data indicate that the two crustal segments have a common intrusive and depositional history from at least 3020 Ma.

In the Cleaverville area, east of Karratha (Fig. 27), tholeiitic amphibolites with MORB-like geochemistry (Ohta et al. 1996: Lithos, 37, 199–221) occur in a greenstone succession containing subordinate chert/banded iron formation and clastic rocks (sandstone, mudstone, and conglomerate) interpreted to have been deposited in an intraplate environment. Influenced by the unpublished results of field mapping by Y. Isozaki, Ohta et al. (1996: op. cit.) interpreted the amphibolite and chert/BIF sequences as tectonically repeated slices of oceanic crust in an accretionary complex associated with the subduction of oceanic lithosphere. According to Hickman (1997: op. cit.), the depositional age of the entire succession is loosely constrained between 3020 and 3260 Ma. Yet the style of tectonism proposed by Ohta et al. (1996: op. cit.) must have postdated deposition of the youngest components (3020 Ma), and therefore have been later than the main sinistral movement on the SSZ. If the alleged accretionary complex was emplaced by 3020 Ma, then some modification to their model is required.

Nd-isotope model ages — tectonic significance of the SSZ and a comparison of Nd model ages between the east and west Pilbara

The oldest dated rocks in the west Pilbara include dacite from the Nickol River Formation near Mount Regal (3251 ± 6 Ma) and the Karratha Granodiorite (3261 ± 4 Ma) near Karratha, north of the SSZ. Their Nd T_{DM} model ages (3430–3480 Ma; Table 3) are 180–220 Ma older than the respective emplacement ages, suggesting that magma generation involved older basement rocks, enriched lithospheric mantle, and/or sedimentary rocks derived from older terrains through subduction. They are also ca 100 Ma or more younger than the Nd T_{DM} model ages of 3520–3670 Ma for some granitoid complexes and rock units emplaced at ~3470 Ma in the east Pilbara, but are similar to the Nd T_{DM} model ages of other units in the east (Table 3). This contrast of Nd model ages between the east and west Pilbara lends support to a model of generally westward growth of the Pilbara Craton (e.g., Krapez 1993: op. cit.). However, we cannot rule out the possibility that some older crust may have existed in parts of the west Pilbara not yet studied.

South of the SSZ in the Roebourne area, felsic igneous rocks of the 3120-Ma Whundo Group have Nd T_{DM} model ages of 3150–3250 Ma, 30–130 Ma older than the emplacement age. Small differences in model and emplacement ages suggest that these rocks were not generated by the melting of ~3260-Ma-type source rocks (e.g., Karratha Granodiorite) north of the SSZ. Instead, they suggest that juvenile crust formed at ~3120 Ma generated the Whundo Group rocks. The same can be said about the 3090–2925-Ma Caines Well Granite Complex to the east. The Cherratta Granitoid Complex (~3100–2925 Ma), which intrudes the Whundo Group in the south of the SSZ, covers a large area and includes several intrusive bodies (e.g., the Gregory Well and Marcia

---
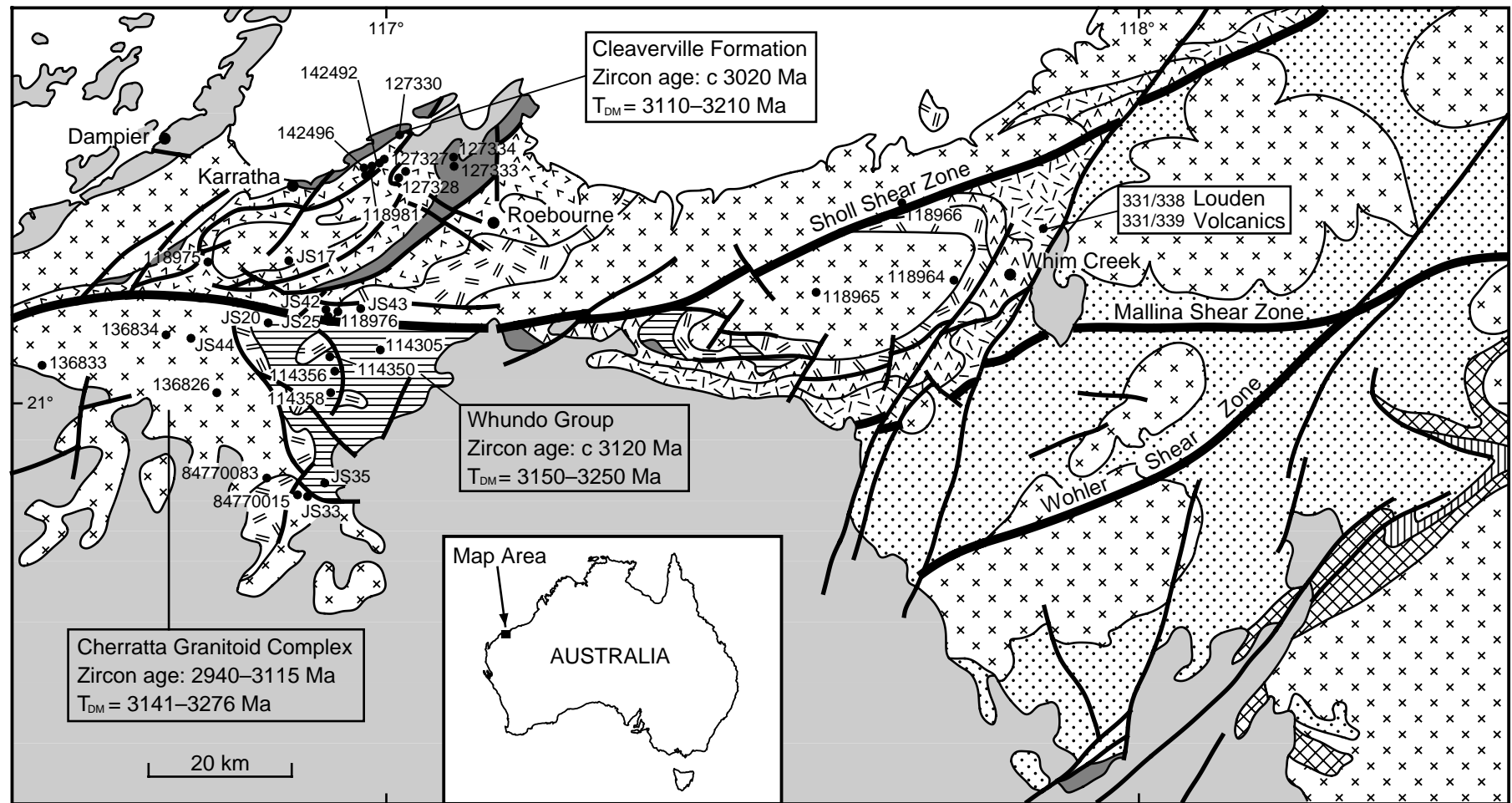
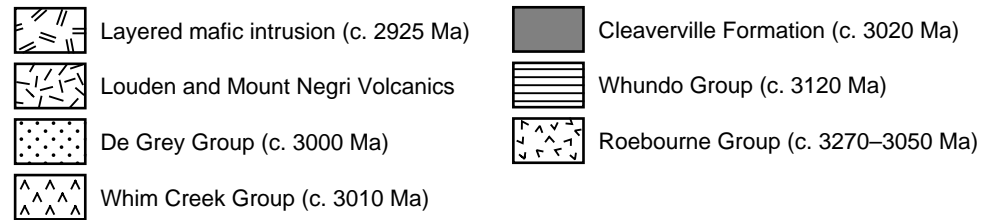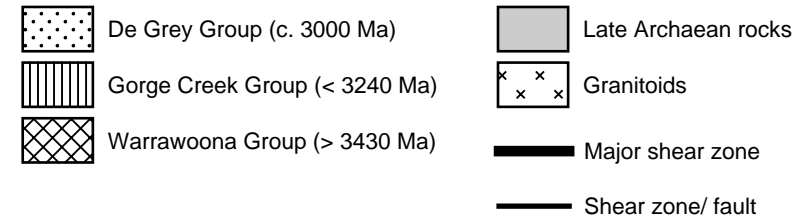**Fig. 27. Simplified geological map of the west Pilbara showing Hickman's (1997: op. cit.) revised stratigraphy, sample locations, and emplacement ages (based on SHRIMP zircon U–Pb ages) and Nd-depleted-mantle model ages (T$_{DM}$) for the main rock units.**

Bore gneisses). They have Nd T$_{DM}$ ages of 3150–3276 Ma, similar to those of the Whundo Goup.

The foregoing data reveal marked contrasts in both emplacement ages of igneous rocks and Nd T$_{DM}$ ages either side of the SSZ. If these differences are further confirmed by Nd-isotope model ages of major units such as the Dampier Granitoid Complex (2997 Ma) to the north of the SSZ, they will lend strong support to the idea that the SSZ separates crustal segments containing different basement rocks. This juxtaposition of contrasting basement rocks could have been achieved by sinistral movement along the SSZ. If so, then the bulk of the Roebourne Group may be dislocated Strelley-type rocks from the east.

In the Cleaverville area, north of the SSZ (Fig. 27), felsic volcanics and dykes emplaced ca 3000 Ma have Nd T$_{DM}$ ages of 3110–3210 Ma (Table 3), a 100–200-Ma difference in common with other samples of ~3000-Ma felsic igneous rocks elsewhere in the west Pilbara. Despite their frequency in the west Pilbara, Nd T$_{DM}$ ages of 3200–3250 Ma are not a simple reflection of the emplacement ages of their source rocks, even though inherited zircons yielding such ages are a common occurrence in younger rocks. Melting of pre-existing 3250-Ma older crust does not explain the generation of these ~3000-Ma igneous rocks with Nd T$_{DM}$ ages of ~3200 Ma; instead, they represent juvenile crust formed after 3250 Ma.

From our Pilbara Craton Nd T$_{DM}$ data (Table 3), we expect that late Archaean felsic igneous rocks (e.g., the 2925-Ma Bookingarra Granite, 2950-Ma Satirist Granite, and 2765-Ma Opaline Well Leucogranite) distributed in areas dominated by 3000–3100 Ma rocks with Nd T$_{DM}$ ages of ~3200 Ma in the west Pilbara would have similar Nd T$_{DM}$ ages if they were generated by melting of these source rocks. This expectation is fulfilled by new data we have obtained for these rocks. In contrast, late Archaean felsic

igneous rocks associated with early Archaean (~3450 Ma) basement rocks in the east Pilbara have correspondingly older Nd T$_{DM}$ ages — ca 3350–3600 Ma or even older (Table 3).

Geochemical arguments for subduction-related processes

The genesis of Archaean calc-alkaline volcanic rocks, some with tonalite–trondhjemite and granodiorite associations, in a subduction zone environment in the Pilbara Craton is open to debate. Unlike many other Archaean terrains in the world where subduction models have been applied, the Pilbara has no single well-defined greenstone belt. Moreover, the various component greenstone belts of the craton show no regional alignment or preferred orientation; instead, most greenstone belt boundaries have been structurally controlled by the emplacement of circular or ovoid granitoid complexes. We suggest that geochemical characteristics of mantle-derived mafic rocks can be used to shed some light on this issue.

The amphibolites with MORB-like geochemistry around Cleaverville were previously studied by Glikson et al. (1986: BMR/AGSO Record 1986/14) and Ohta et al. (1996: op. cit.). Ohta et al. suggested that they and their associated cherts and clastic rocks represent an accretionary complex generated by the subduction of oceanic lithosphere. Our new geochemical (ICP–MS) data confirm the MORB-like features of these amphibolites (Fig. 28). Later mafic dykes (ca. 3000 Ma?) intruding them evince strong light REE, Th enrichment, and Nb depletion, similar to ~3.0-Ga high-magnesian basalts of the Louden Volcanics (Fig. 28; mistakenly called 'Negri Volcanics' by Sun et al. (1989: *in* A.J. Crawford, Editor, Boninites and related rocks, Unwin Hyman, 148–173). Samples of the Louden Volcanics have an

initial εNd value of –1.8 at 3.0 Ga, which is considerably lower than that (~+3) of the depleted mantle at that time and of some of the Cleaverville amphibolites. A reasonable explanation for this low initial εNd value and trace-element spidergram pattern of the Louden Volcanics is that the mantle source was contaminated by sediments derived mainly from ~3250-Ma source rocks in the region. We suggest that mantle sources of ~3.0-Ga mafic dykes in the Cleaverville area have also been modified by subduction processes (Sun, Nakamura, & Hickman, research in progress). Similarly, geochemical data for basalts in the Whundo Group (Glikson et al. 1986: op. cit.) are consistent with juvenile crust generated in a subduction zone environment (as suggested by Smith et al. in press: op. cit.).

The geochemical characteristics of the ~3.0-Ga Louden Volcanics and mafic dykes cutting Cleaverville MORB-like amphibolites are shared by other light-REE-enriched Archaean mafic igneous rocks in the Pilbara, including 2760–2690-Ma Fortescue Group flood basalts (Fig. 28). Nelson et al. (1992: Precambrian Research, 54, 231–256) suggested that the Fortescue flood basalts were generated in an intraplate environment through interaction of asthenospheric mantle plumes with lithospheric mantle meta-somatised by a subduction zone process several hundred millions of years before 2.7 Ga. A literature survey indicates that basalts from various parts of the Pilbara have geochemical features consistent with subduction-related environments. Some of the better examples offer strong support for the idea that lithospheric plate subduction is an important process in crustal growth of the Pilbara Craton.

A corollary of this consideration concerns the tectonic environment of volcanic-hosted massive sulphide (VMS) deposits associated with Archaean volcanic sequences. In some of these deposits, basalts have trace-element characteristics, such as Nb and Ta

Table 3. Comparison of Nd model ages and emplacement ages of igneous rocks between the east and west Pilbara

Location	Emplacement age (Ma)	εNd_I	T_{DM} (Ma)	$T_{DM} - T$ (Ma)	Data sources
East Pilbara					
North Shaw regional suite	3470	1.7 to –0.5	3520–3670	50–200	McCulloch (1987); Bickle et al. (1993)
Duffer Formation	3460	0.6	3590	130	McCulloch (1987)
Mount Edgar Granitoid Complex	3310	0.6	3460	150	McCulloch (1987)
Boobina Porphyry	3305	0.4	3466	161	McCulloch (1987)
Bamboo Springs pluton	2950	–2.8	3380	430	Bickle et al. (1989)
Mulgadinnah Hill leucoadamellite	2943	–4.0	3462	519	Bickle et al. (1989)
Pilga Station leucoadamellite	2943	–4.1	3470	527	Bickle et al. (1989)
Garden Creek adamellite	3007	–4.3	3537	530	Bickle et al. (1989)
Kurrana Downs Granitoid Complex	2900	–3.2	3372	472	Tyler et al. (1992)
Ballinooka inlier, post-tectonic granite	2900	–1.0	3220	320	Tyler et al. (1992)
Cooglegong Adamellite, Shaw Granitoid Complex	2850	–4.2 to –8.0	3390–3650	540–800	Bickle et al. (1989)
West Pilbara					
North of SSZ					
Karratha Granodiorite, Harding Granite, and Mount Regal dacite (JS17, JS43, 118975)	ca 3260	0 to –0.4	3430–3480	170–220	This study; Smith et al. (in press)
Nickol River dacite, lower succession (118976)	3023	–0.6	3298	275	This study
Felsic porphyry in Regal Basalt (127327, 127328), Cleaverville Fm (127333, 127334), Lagoon rhyolite (118981)	ca 3000	0.4 to 1.8	3110–3210	110–210	This study
Louden Volcanics (331/338, 331/339)	ca 3000	–1.8	3368	ca 370	Sun et al. (1989)
Forestier Bay gneiss (118966)	3014	–0.4	3276	262	This study
Sholl Shear Zone (JS25, JS42)	3024	–0.9 to –1.5	3316–3355	292–331	Smith et al. (in press)
South of SSZ					
Whundo Group volcanics (114305, 114350, 114356, 114358, JS20)	3120	1.3 to 2.6	3150–3250	30–130	This study; Smith et al. (in press)
Cherratta Granitoid Complex (JS33); Marcia Bore gneiss* (136833), Gregory Well gneiss* (136834)	3115	0.8 to 2.6	3141–3276	26–161	Smith et al. (in press); this study
Sholl belt (JS 35)	3013	0.5	3211	198	Smith et al. (in press)
Cherratta Granitoid Complex (136826, 84770115, 84770083, JS44),	2990	0.2 to 0.9	3150–3215	160–225	This study; Sun & Hoatson (1992); Smith et al. (in press)
Caines Well Granitoid Complex (118965)	3093	2.8	3118	25	This study
Bookingarra Granite (118964)	2925	0.1	3164	239	This study

Additional references: Bickle et al. (1989: Contribution to Mineralogy & Petrology, 101, 361–376); Bickle et al. (1993: Precambrian Research, 60, 117–149); McCulloch (1987: American Geophysical Union, Geodynamics Series, 17, 115–130); Sun & Hoatson (1992: AGSO Bulletin 242, 141–149); Tyler et al. (1992: Precambrian Research, 54, 211–229).

* On the basis of field occurrence and chemical composition, we suggest that the Marcia Bore and Gregory Well gneisses belong to the 3100-Ma age group.

depletion and Th and Ba enrichment (cf. Fig. 28), which may be generated by subduction zone processes. However, an island-arc or cordilleran environment is not essential for the generation of these basalts; rather, many basalts originating in an intraplate environment, such as the Fortescue Group basalts, could have had their mantle source regions modified by prior subduction processes. A closer examination of all pertinent geological information and an integrated interpretation of the data might reveal the evidence for such processes.

[1] Minerals Division, Australian Geological Survey Organisation, PO Box 378, Canberra, ACT 2601; tel. +61 2 6249 9484; fax +61 2 6249 9983; e-mail ssun@agso.gov.au.

[2] Geological Survey of Western Australia, 100 Plain Street, East Perth, WA 6004; tel. +61 8 9222 3220; fax +61 8 9222 3633; e-mail a.hickman@dme.wa.gov.au.
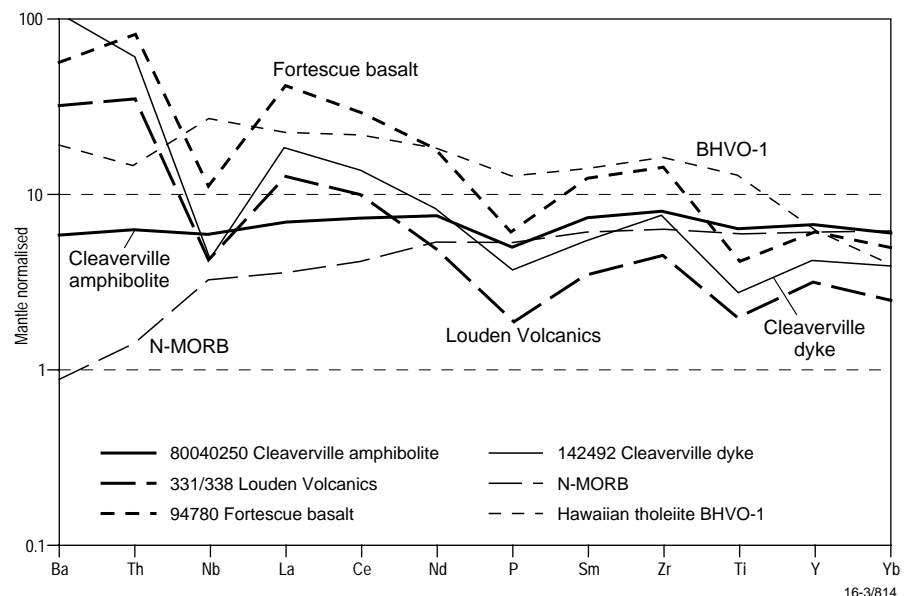
Fig. 28. Mantle-normalised trace-element diagram for MORB-like Cleaverville amphibolite; ~3.0-Ga high-magnesian Louden Volcanics; later mafic dykes intruding Cleaverville amphibolites; and 2760–2690-Ma intraplate Fortescue Group flood basalts (showing strong light REE, Th enrichment, and Nb depletion).

Basement studies in basin analysis: new insights into the evolution of the Lawn Hill Platform

Deb Scott[1], Chris Tarlowski[1], Rod Page[1], Mart Idnurm[1], Dave Rawlings[2], M.J. (Jim) Jackson[1], & Doug Mackenzie[1]

Why are basement studies important to a basin analysis? How can an understanding of the basement template assist stratigraphic analysis? How do we define basement?

We address these questions through an example of an integrated basement analysis that provides a new interpretation of the basement template underlying the northern Lawn Hill Platform (NLHP)

between the outcropping basement Murphy Inlier and the world-class Century Zn deposit. The interpretation requires a revision of traditional correlations of igneous units from the
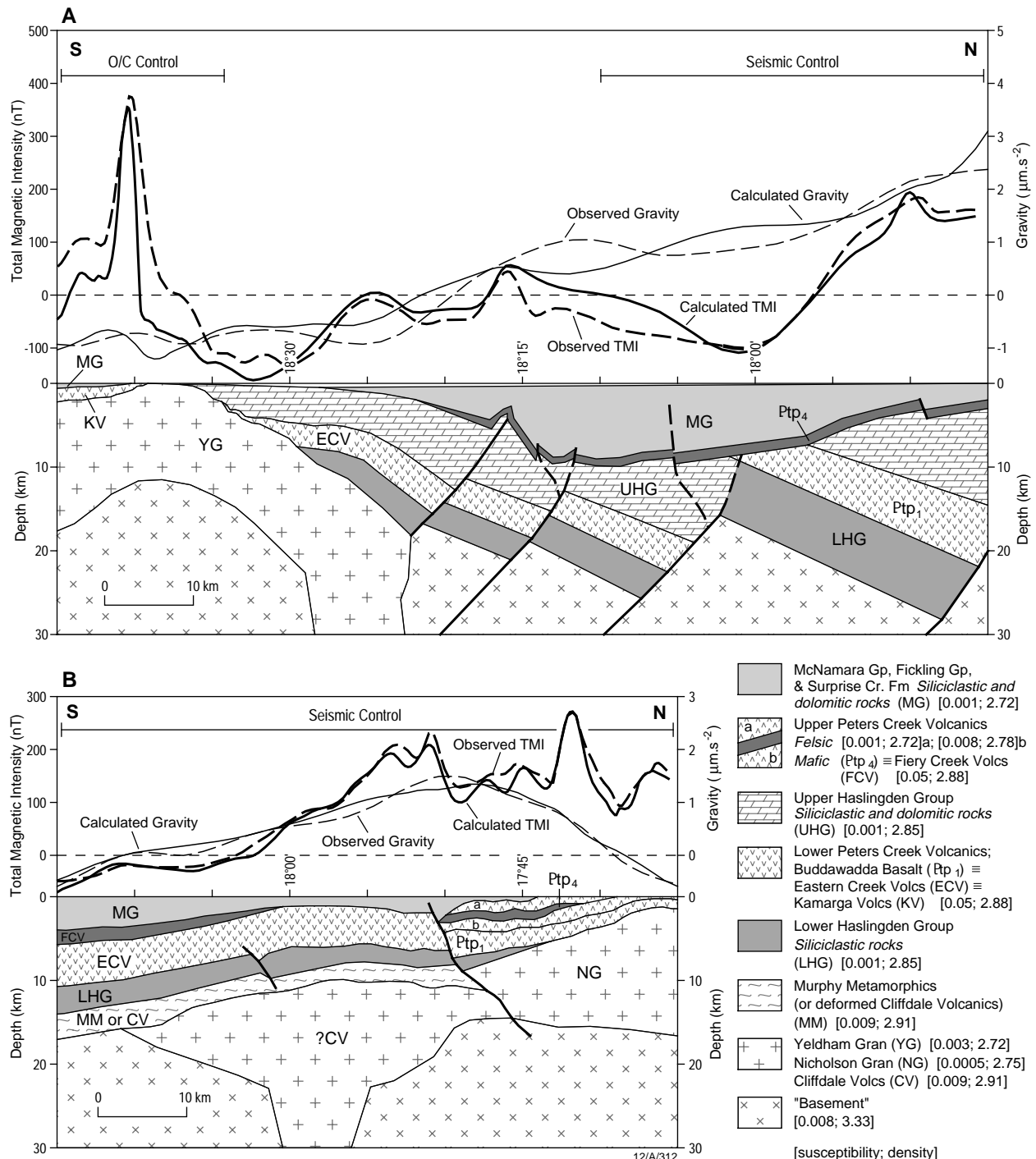

Fig. 29. Geological models derived from both seismic data and outcrop geology are forward-modelled and compared with observed magnetic and gravity profile data. The upper (eastern) profile extends from latitude 17°45'–18°45' along longitude 139°00'. The lower (western) profile extends from latitude 17°35'–18°15' along longitude 138°30'. Note the distinctly discordant relationship between the older and younger igneous units in the eastern profile and the broadly conformable relationship between them in the western profile. Correlation of the various igneous units as shown is consistent with geochronological, geochemical, palaeomagnetic, and recently obtained outcrop relationship data.

period ~1760–1710 Ma. It also provides new insights into the evolution of the overlying Palaeoproterozoic basin phases and models of mineralisation within them.

Sedimentary basins are rarely underlain by homogeneous crystalline igneous basement. Instead, basement rocks are commonly heterogeneous and a product of a series of geological processes, including previous basin formation. The two geological models in Figure 29 suggest that basement underlying the NLHP is no exception. A rare opportunity to constrain basement interpretations exists in the NLHP because all the primary datasets normally used in basement analysis are available: outcrop geological, geopotential, geochronological, geochemical, and palaeomagnetic data. Additionally, and importantly, limited reflection seismic data from petroleum exploration which directly image subsurface structures are also available for the southern flank of the Murphy Inlier (Fig. 31). The basement interpretation draws on regional datasets in AGSO's national databases combined with additional data collected during the 'North Australian basins resource evaluation' (NABRE) project.

Identifying basement

Immediately south of the Murphy Inlier, the seismic data image a southward-thickening sedimentary megawedge (MG; Fig. 29) above a sharp acoustic basement. The megawedge is divided into nine supersequences (not shown in Fig. 29) on the basis of internal characteristics representing distinct basin phases (Scott & Bradshaw 1997: abstract in AGSO Record 1997/12). The packages within the megawedge are correlated with the McNamara Group and the Surprise Creek Formation in the south and with the Fickling Group in the north (Bradshaw et al. 1996: abstract in Baker et al. (Editors), MIC '96: New developments in metallogenic research, the McArthur–Mt Isa–Cloncurry minerals province, Townsville, April 22–23, 20–23; Bradshaw & Scott 1997: abstract in AGSO Record 1997/12). This interpretation differs substantially from the previous correlation of the lower third of the megawedge with the Peters Creek Volcanics (PCV; McConachie et al. 1993: APEA Journal, 33, 237–257). The

acoustic basement reflection is attributed to the top of the Fiery Creek Volcanics (FCV), which underlie the McNamara Group and Surprise Creek Formation in the south. However, outcrop ties require the reflectivity be attributed to the PCV at the northern limits of most western seismic lines. Correlation of these two igneous assemblages is enigmatic, as the isotopic ages of their felsic portions differ by 15 m.y. (Fig. 30). A reconciliation is proposed in the geological models in Figure 29.

What is the basement under the megawedge? How does the igneous record in the north correlate with that in the south? What is the structural template of the basement? Did the basement template influence subsequent basin evolution?

Depth contours on the base of the megawedge calculated from the seismic data follow contours of the magnetic image, but do not deepen sufficiently to account for the large magnetic low that extends southeast from latitude 18°00'S, longitude 139°00'E (Fig. 31). Thus, the assumption of a magnetic layer at the depths of the southward-deepening acoustic basement does not successfully reproduce the observed geopotential data.

A series of magnetic and gravity profile data were extracted from the gridded and reprocessed image data across and extending south of the Murphy Inlier (e.g., Leven et al. 1997: abstract in AGSO Record 1997/12; Scott et al. 1997: abstract in AGSO Record 1997/12). Various models were constructed to investigate the relationship between igneous units and associated basin rocks away from the Murphy Inlier. Two meridional profiles illustrate the most significant results of this study (Fig. 29). The geometries (i.e., depth and dip) of the geological models are constrained by interpretations of relevant seismic data (Scott & Bradshaw 1997: op. cit.). The observed data along the profiles require different magnetic body geometry below a volcanic unit at acoustic basement depths.

Local coherent reflections below the interpreted base of the megawedge provide some evidence of the geometry of heterogeneities within the basement. Geological models derived from Scott & Bradshaw's (1997: op. cit.) interpretation

of the seismic data are forward-modelled to reproduce observed gravity and magnetic data (Fig. 29). The best-fit geological models suggest that there were two igneous events separated by a major extensional event. The extension produced a marked angular unconformity between the two igneous packages in the east, while maintaining a broadly conformable relationship in the west.

The modelling suggests that acoustic basement in the east is the top of the thinner, younger mafic igneous unit, and that the older unit is discordant. However, in the west, the units are broadly concordant, and acoustic basement may alternate between them along the profile. The profile models require a polarity switch in the extensional basement system (Fig. 31). The extension is interpreted to have been accommodated by west-northwesterly to northwesterly normal faults and north-northeasterly to northeasterly transverse faults.

Basement igneous correlations

The seven members of the PCV (Ptp$_{1-7}$; Fig. 30) traditionally have been assumed to be a broadly coeval, sequential bimodal system, including minor sedimentary packages, but recent fieldwork has revised their outcrop relationships. A major unconformity was identified and traced laterally along the southern flank of the Murphy Inlier between the basal mafic unit (Ptp$_1$) and the rest of the bimodal pile. The pile above the unconformity contains both intrusive and extrusive bimodal igneous rocks and thin sedimentary units that are not necessarily sequential in age (e.g., Ptp$_2$ is intrusive and younger than Ptp$_3$; Fig. 30). Ptp$_1$ is intensely altered and is distinct from fresher dolerite (Ptp$_{1i}$) that intrudes it. Palaeomagnetic and geochemical data are reconciled by this new outcrop information (e.g., the pole from Ptp$_{1i}$ is younger than the pole determined for the Lochness Formation, and the geochemical affinity of Ptp$_{1i}$ is with igneous units younger than Ptp$_1$). Definitive stratigraphic correlation of Ptp$_3$ with the lower Wollogorang Formation to the north has been made on the basis of a distinctive suite of sedimentary facies including stromatolites. The lower Wollogorang Formation has been dated

at ca 1730 Ma (Page 1997: abstract in AGSO Record 1997/12).

In the southern Mount Isa Inlier (Blake 1987: BMR/AGSO Bulletin 225; Stewart & Blake 1992: AGSO Bulletin 243), the Haslingden Group contains the Eastern Creek Volcanics (ECV) and several kilometres of overlying siliciclastic and minor carbonate sedimentary rocks. The ECV constitute a 6–8-km package of continental flood basalts without any known associated felsic rocks (Bain et al. 1992: in Stewart & Blake op. cit.). Overlying the top of the Haslingden Group (the Lochness Formation), the Quilalar Formation is a quartzite and carbonate unit with thin mafic units in both upper and lower stratigraphic positions.

The type section of the FCV is stratigraphically above both the ECV and Quilalar Formation locally. At some locations, the FCV and the underlying siliciclastic Bigie Formation directly overlie the Lochness Formation with a pronounced angular unconformity. The mapped FCV is generally poorly developed in areas where the Quilalar Formation is preserved. However, in those areas that were visited during the fieldwork a thin mafic unit in the upper part of the mapped Quilalar Formation is frequently underlain by a conglomeratic lithic sandstone that is sedimentologically similar to the Bigie Formation.

Recent field investigations and the combined data summarised in Figure 30 suggest that the PCV pile contains representatives of both regionally recognised mafic igneous events that were initiated at ~1750 Ma (Ptp_1 = ECV) and ~1730 Ma (Ptp_{1i}, Ptp_4, Ptp_6 = FCV ± Quilalar Formation mafic rocks). Intrusive (and extrusive) felsic igneous activity associated with the younger event continued sporadically for at least 20 m.y. (ca 1729–1709 Ma), apparently ceasing earlier in the north than in the south. The thick basin sediments of the upper Haslingden Group that separate the two igneous events in southern outcrops were probably not deposited in the northwest, or were subsequently eroded.

Basement influences on basin development

Regional extension at ca 1730 Ma produced opposing-polarity half-graben in the basement of the NLHP. The resulting basement template had an enduring influence on subsequent basin evolution. Scott & Bradshaw (1997: op. cit.) have interpreted three major tectonic events which affected depositional geometries of the basin phases within the megawedge:

• local, structurally controlled deeps of the extensional to transtensional ca 1640-Ma event developed adjacent to north-northeasterly trending ca 1730-Ma transverse structures;
• likewise, bends in ca 1595-Ma west-northwesterly trending wrench structures localised over older structures produced both negative and positive flower structures; and
• finally, late-stage (<1580 Ma) conjugate joints, probably associated with the initial stages of the Isan Orogeny, are focused and more densely spaced over the earlier structures.

These late stage joints have been postulated to be the primary conduits for mineralising fluids responsible for the Century Zn deposit (Broadbent 1996: abstract in Baker et al. (Editors) op. cit.).

NORTHERN Megawedge		Extrusive	Intrusive	Felsic	Mafic	Sediment	Geochem	Paleomag	Geochron (Ma)	SOUTHERN Megawedge
		X	X	X			G3		1709±3	FCV
	Ptp_7	X		X			G3	P2b	1724±2	
	Ptp_6	X	X		X	X	G2	P2b		
Peters Creek Volcanics (PCV)		X	X		X	X	G2	P2c		FCV
	Ptp_5		X	X			G3	P2b		
	Ptp_4	X			X					Quilalar Fm
		?X	?X		X	X				
	Ptp_3					X			~1730±4	
	Ptp_2		X	X			G3		1726±2 1729±4	
	Ptp_{1i}		X		X		G2	P2a		Lochness Fm
	uncon					X		P1		
	Ptp_1	X			X		G1	P(op)		
		X			X		G1			ECV

12/A/313

Fig. 30. Comparison of historical and recent NABRE geochronological, geochemical, palaeomagnetic, and geological data for the igneous associations from the north and south outcrop belts. The basement interpretation of the NLHP requires a revision of traditional correlations between the two belts. Geochemical data are grouped (G1–G3) by compositional affinities (D.E. Mackenzie, AGSO, unpublished report). Paleomagnetic poles are labelled with a relative age (1>2, a>b>c) as determined by their positions on the apparent polar-wander path (Idnurm et al. 1995: Precambrian Research, 72, 1–41; Idnurm 1997: abstract in AGSO Record 1997/12; M. Idnurm, AGSO, unpublished data); P(op) = overprint, no primary pole is available; the P2c pole of the FCV appears to be younger than the Ptp_{5-7} P2b pole; the sample was obtained from a section where no Quilalar Formation or felsic FCV are preserved. Geochronological data are obtained from U–Pb SHRIMP analysis of samples from the indicated units, except for Ptp_3, which is estimated from ages obtained from correlatives (see text); ages are from Page (1988: Precambrian Research, 40/41, 1–19), Page (1997: abstract in AGSO Record 1997/12), Page & Sweet (in press: Australian Journal of Earth Sciences), and R.W. Page (AGSO, unpublished data); the 1709-Ma date for the FCV was obtained from a unit whose map relationships suggest it is a very late-stage intrusion. uncon = unconformity established by recent fieldwork. X = major component or mode of emplacement; x = minor component or mode of emplacement.

Conclusion

Understanding the basement template has significant impact on how we model subsequent basin evolution and fluid flow histories. Importantly, geometries that produce perfect fits to geopotential data are not adequate to help constrain models because they can produce implausible geological cross-sections. A multidisciplinary integration of all data to produce realistic geological models of the basement is required. Radically different fluid flow

patterns, aquifer geometries, and burial histories of potential metalliferous source rocks are predicted by the opposing-polarity half-graben in the basement of the NLHP. Similarly, the structural interconnectivity of any plumbing system and tapping of deep fluids cannot be fully modelled without an understanding of the basement template.

Basement under the NLHP is not homogeneous. It is a complex assemblage of a variety of rock types of different ages and structural heterogeneities. Understanding the nature of the influence of the underlying basement template in the NLHP has contributed to the identification of a major base-metal prospect in Century host-rock equivalents (Bradshaw et al. 1998: AGSO Record 1998/4).

[1] Minerals Division, Australian Geological Survey Organisation, GPO Box 378, Canberra, ACT 2601; tel. +61 2 6249 9443 (DS), +61 2 6249 9265 (CT), +61 2 6249 4261 (tel. & fax for RP), +61 2 6249 9205 (MJJ), +61 2 6249 9281 (DM); fax +61 2 6249 9956; e-mail dscott@agso.gov.au, ctarlows@agso.gov.au, rpage@agso.gov.au, jjackson@agso.gov.au, dmackenz@agso.gov.au.

[2] Centre for Ore Deposit Research (CODES SRC), Geology Department, University of Tasmania, GPO Box 252-79c, Hobart, Tasmania 7001; tel. +61 3 6226 7155, fax +61 3 6226 7662, e-mail D.Rawlings@utas.edu.au.

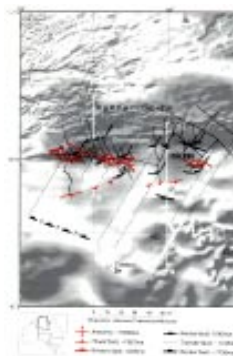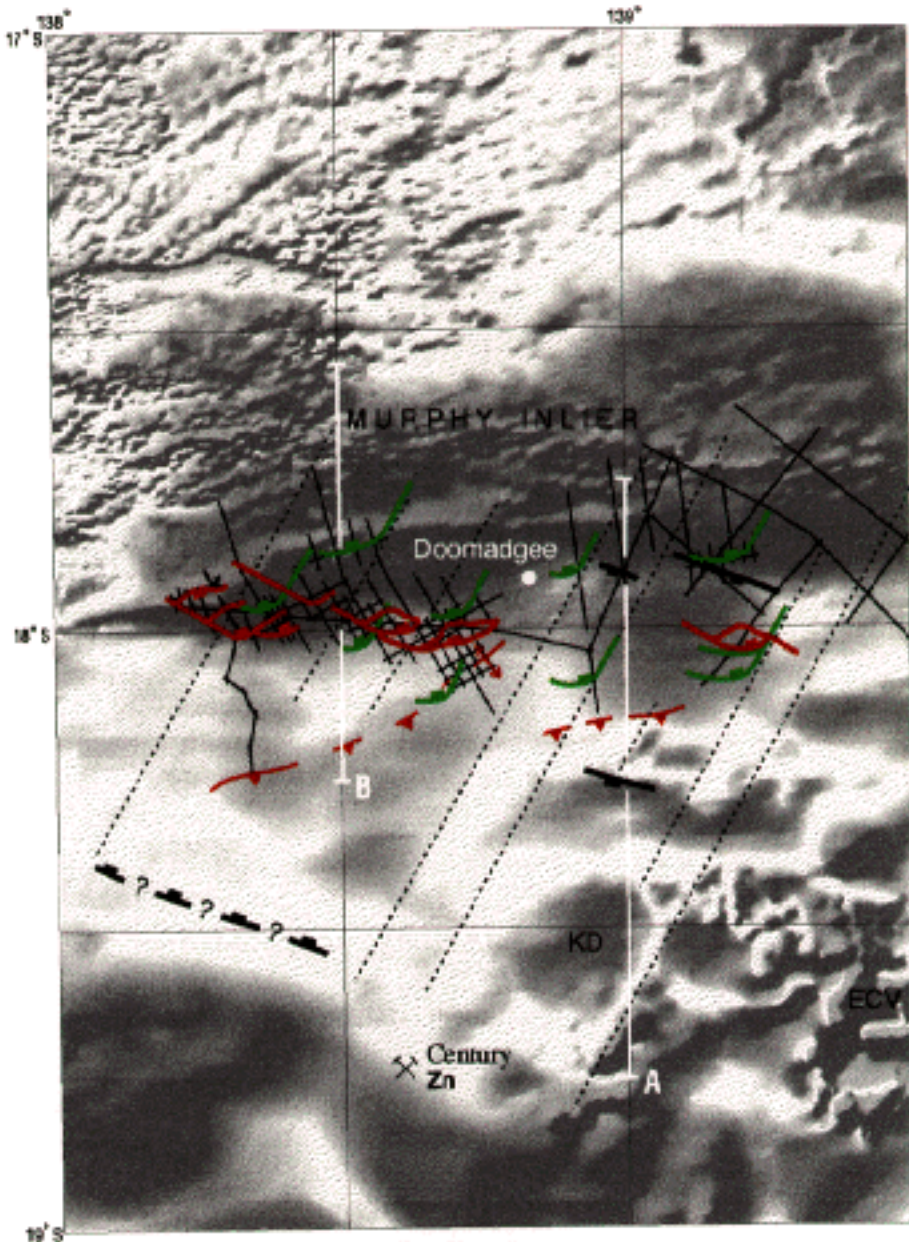*Click on this image for a larger version (116k)*

Fig. 31. Simplified fault map of the northern Lawn Hill Platform (NLHP) underlain by greyscale TMI (total magnetic intensity, reduced to the pole) data, and showing a plan view of the spatial relationships of various deformation events. A broad north-northeasterly trending zone in the basement system (~1730 Ma) extends across the NLHP and appears to transfer extension from southward-dipping bounding faults in the northeast to northward-dipping bounding faults in the southeast. The world-class Century Zn deposit is positioned at the southern extent of the polarity-reversing structure. The basement system appears to influence the geometry and distribution of later deformation events (at 1640 and 1595 Ma). A and B are the locations of geological models presented in Figure 29. The locations of seismic profiles on the southern flank of the Murphy Inlier are shown as solid black lines. The broad ~east–west long-wavelength magnetic anomaly of the Murphy Inlier extends across the entire study area, beyond the limited outcrop belt at the northwest limit of the seismic grid. The high-frequency magnetic signature in the southeast corresponds to outcropping Eastern Creek Volcanics (ECV). The Kamarga Dome (KD) is cored by the ancient Yeldham Granite (see profile A, Fig. 29). The small inset shows the locations of the NABRE project area and NLHP.

Symbol	Description
Anticline, <1580ma	Normal fault, 1640ma
Thrust fault, <1580ma	Transfer fault, ~1730ma
Wrench fault, 1595ma	Normal fault, ~1730ma

Scale: 0 10 20 30 40 50 km

Projection: Universal Transverse Mercator

MURPHY INLIER

Doomadgee

Century Zn

KD

ECV

B

A

17°S 138° 139°

18°S

19°S